Schedule for Presentation Meeting of Master-Degree Thesis in 2016
International Program of Maritime & Urban Engineering

Date : July 26 (Tuesday) starting from 10:00
Venue : S1-312 Lecture Room

No.	Time	Name	Supervisor	Title of thesis	Chairman
1	10:00 – 10:25	Wardi Syafri	Sanada	Shear Performance of RC Columns with Wide Hoop Spacing at Mechanical Splices	Kashiwagi
2	10:25 – 10:50	Han Htoo Htoo Ko	Fujikubo	Collapse Analysis of Ship Hull Girder Using Idealized Structural Unit Method	Kashiwagi
3	10:50 – 11:15	Thet Zaw Htet	Umeda	Probabilistic Prediction of Broaching and Broaching-induced Roll for Ships with Twin Propellers and Twin Rudders	Kashiwagi
4	11:15 – 11:40	Muhajjir	Aoki	Study on Sediment Transport around Lampulo Fishing Port on Banda Aceh Coast	Kashiwagi
Lunch Break					
5	13:00 – 13:25	Wicaksono Ardhana	Kashiwagi	Wave-Induced Steady Forces and Seakeeping Performance of an Advancing Ship in Oblique Seas	Kita
6	13:25 – 13:50	Truong Quang Tho	Toda	The EFD and CFD Study of the Bulbous Rudder with Asymmetric Horizontal Fins with Different Angles of Attack in Ship and Propeller Wake Field of KVLCC2 Tanker	Kita
7	13:50 – 14:15	De Gracia Claude Luis Carlos	Osawa	A Study on Influence of the Difference in Heading Models on Fatigue Assessment Results	Kita
Break					
8	14:30 – 14:55	Ruiz Valdes Hector Olmedo	Osawa	Prediction of Distortion Produced in Welded Structures during Straightening Process using the Inherent Strain Method	Doi
9	14:55 – 15:20	Dewantara Ryan Putra	Suzuki	Guidance and Control of Autonomous Underwater Vehicle SOTAB-I and Its Application to Data Assimilation	Doi
10	15:20 – 15:45	Pinzon Acosta Cesar De Jesus	Hasegawa	Artificial Neural Network Application for Parameter Prediction of Heat Induced Distortion as an Inverse Problem	Doi
11	15:45 – 16:10	Felipe Rodrigues Modesto	Toda	The Influence of Side Hull Location and Ship Speed on the Ship Wave Pattern of a Trimaran with Wigley Hull Form	Doi

Meeting for Evaluation: From 16:30 at S1-323 Meeting Room
Members are Steering committee members and the supervisors

Shear Performance of RC Columns with Wide Hoop Spacing at Mechanical Splices

Syafri Wardi
Concrete Structure Laboratory, Department of Architecture Engineering

Key Words: *Reinforced concrete, Mechanical splice, Shear strength, Performance evaluation, Structural test*

1. Introduction

The application of a mechanical coupler to screw thread bar jointing has steadily expanded in recent years because of its simple installation. However, there are some problems in the application of this type of jointing to reinforced concrete (RC) members. The shear reinforcements must be placed on the couplers to satisfy the minimum spacing demand, as shown in Fig. 1.a. Consequently, in the construction process, different sizes of hoops/stirrups must be considered on and off the couplers because they have a larger diameter than the longitudinal reinforcement. Moreover, in practical design, when the hoops/stirrups are placed on the couplers, the longitudinal reinforcements may be rearranged on the inner side to satisfy the minimum concrete cover demand, which results in a loss of flexural resistance. Therefore, it will be effective for both practical design and construction to intensively arrange the hoops/stirrups at both ends of the mechanical couplers, as shown in Fig. 1.b, if its negative effects are appropriately evaluated.

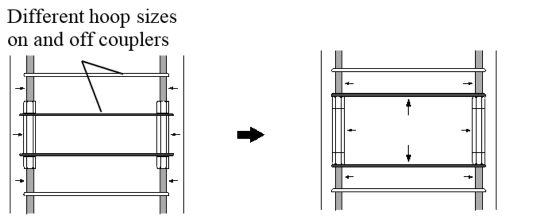

(a) Conventional arrangement (b) Proposed arrangement

Fig. 1 Conventional and proposed hoop arrangement.

The same type of hoop arrangement was proposed and applied to precast concrete members with splice sleeve joints at the member ends[1]. The behavior appeared to be affected by both shear and bending moments because the splice sleeve joints were placed at the member ends. In contrast, in the current study, mechanical couplers with relatively shorter lengths were installed in cast-in-place RC members beyond the plastic hinge regions, which may limit the negative effects on the shear performance. The intensive stirrup arrangement was also applied to cast-in-place RC beams and experimentally verified the low shear performance reduction[2]. This study focuses on the applicability of the intensive hoop arrangement to cast-in-place RC columns.

2. Experiments of Shear-Critical RC Columns with Wide Hoop Spacing at Mechanical Splices

2.1. Specimens and Loading System

Sixteen shear-critical column specimens with a scale of 1/2 were prepared. Eight columns were designed with continuous longitudinal reinforcements functioning as benchmark specimens. The other eight columns were designed using mechanical couplers for jointing longitudinal reinforcements in which hoops are moved to the top and bottom ends of the couplers, as shown in Fig. 1.b.

All of the couplers in these columns were placed at the middle height to simulate typical construction conditions. The experimental parameters included the absence or presence of coupler jointing, shear span-to-depth ratios of 1.0, 1.5, and 2.0, and shear reinforcement ratios of 0.3, 0.6, and 1.2.

Displacement-controlled reversed cyclic loads were applied to the specimens using a horizontal jack under a constant axial load equal to 20% of the column compressive strength applied by two vertical jacks.

2.2 Experimental Results

All specimens exhibited the shear failure mode. Comparing the failure processes between the specimens without and with mechanical couplers which have the same shear span ratio and shear reinforcement ratio exhibited almost similar behavior: initial bending cracking, shear cracking, bonding cracking, and yielding of shear reinforcement prior to that of longitudinal reinforcement.

The maximum strengths of several columns with couplers decreased slightly from the wide hoop spacing at mechanical splices. The maximum reduction of the shear strengths of columns with couplers was observed approximately 12% lower compared to that of without couplers. The specimens with the highest shear reinforcement ratio were more significantly affected because the spacing of the normal shear reinforcement was considerably smaller than the coupler length. Therefore, structural indices considering the wide hoop spacing are proposed in the following chapter.

3. Shear Strength Evaluation of Shear-Critical RC Columns with Wide Hoop Spacing at Mechanical Splices

3.1. Previous Shear Strength Models

Many researchers have proposed shear strength models for RC columns over the past few decades. Three existing models were evaluated in this study: the Japanese Design Guideline AIJ 1990 model[3], revised UCSD model[4], and ASCE/SEI 41-06 model[5].

3.2. Proposal of Indices to Consider Wide Hoop Spacing

Two variables were proposed to consider the effects of the wide hoop spacing at mechanical splices: an equivalent area of shear reinforcements (A_{ve}) and an equivalent spacing between shear reinforcements (s_e).

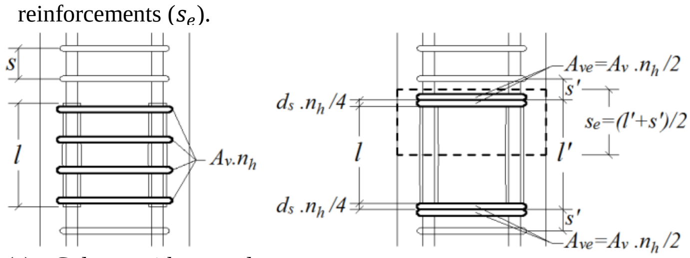

(a) Column with normal hoop spacing at mechanical splices (b) Column with the wide hoop spacing at mechanical splices

Fig. 2 Proposed variable.

The proposed variables were defined as the following equations as well as shown in Fig. 2:

$$A_{ve} = A_v . n_h / 2 \tag{1}$$
$$s_e = (l' + s')/2 \tag{2}$$

where A_v is area of a set of normal hoop; n_h is the number of hoops intensively arranged (moved from the joint region); $l' = l + d_s . n_h / 2$; d_s is diameter of hoops; and s' is the spacing between the centers of intensive hoops and normal hoops.

The proposed indices are applied to replace A_v and s (spacing of normal hoops) in revised UCSD model and ASCE/SEI 41-06 model and to replace the shear reinforcement ratio $p_w = A_{ve}/b.s_e$ in AIJ 1990 model, where b is the column width.

3.3. Applicability of the Proposed Indices to Shear Strength Evaluation

The shear strengths of the column specimens were evaluated by the previous shear strength evaluation models with and without consideration of the proposed indices. Focusing on the normal columns without couplers, the revised UCSD model resulted in the best agreement with the experimental strengths, whereas both AIJ 1990 and ASCE/SEI 41-06 models resulted in underestimations. The revised UCSD model was selected for the following shear strength evaluation in this study. The application of the proposed indices to this model provided the mean value of ratio of experimental to calculated strength of 0.99 with coefficient of variant of 0.08.

4. Experiments of Ductile RC Columns with Wide Hoop Spacing at Mechanical Splices

4.1. Specimens and Loading System

Six specimens with a scale of 1/2 were designed to investigate the applicability of the proposed evaluation method to practical shear design for ductile columns. Four columns had coupler jointing placed out of plastic zone, one specimen had coupler jointing with overlapping with the plastic zone at 1.0 D from the end of column, and one specimen had continuous longitudinal reinforcements without splices. All specimens had the shear span-to-depth ratio of 1.5. A common arrangement of longitudinal reinforcements was applied to all columns. The specimens were designed with variations in the shear reinforcement ratio from 0.3% to 1.3%. All specimens were expected to yield in flexure prior to failing in shear.

The specimens were subjected to varying axial loads, which were controlled by the applied lateral loads. An initial axial load was equal to 10% of the column compressive strength representing the long-term axial stress of the column. The axial load was varied up to ± 15%, which resulted in total axial loads of -5% and +25% of the compressive strength in tension and compression, respectively, considering a realistic axial load range for typical exterior columns.

4.2. Experimental Results and Discussions

The specimens exhibited flexure-shear failure and ductile flexural failure. The specimens with the same amount of shear reinforcement, exhibited similar experimental behavior and performance. However, the joint located closer to the flexural hinge at the column bottom reduced the ultimate displacement by approximately 4% compared to that of those with joint located out of plastic zone.

5. Seismic Performance Evaluation of Ductile RC Columns with Wide Hoop Spacing at Mechanical Splices

Seismic performance of RC columns can be estimated by combining the shear strength envelope with the flexural capacity envelope. The shear capacity was obtained using the revised UCSD model while applying the proposed indices in Sections 3.2. The column flexural performance was idealized in a typical manner for conventional columns without a mechanical coupler. The ultimate displacement of the flexure-dominated columns were estimated as a displacement at the onset of longitudinal reinforcement buckling[6]. Figure 3 compares the calculated shear and flexural performance curves with the skeleton curves from the experiments.

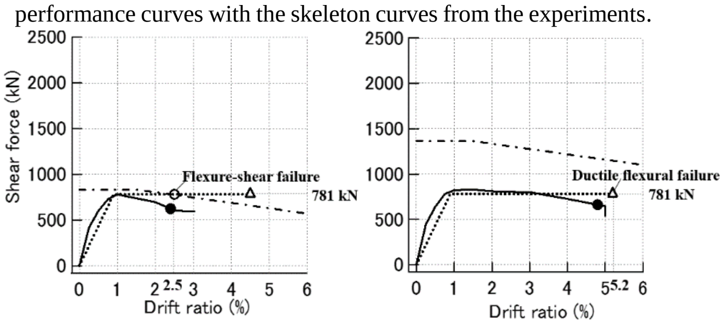

(a) Flexure-shear column (b) Flexure-column

Skeleton curve (experiment)
Idealized flexural response (estimated)
Shear capacity (revised UCSD model applied the authors' proposed indices)
Ultimate displacement (experiment)
Ultimate displacement (estimated for flexure-shear column)
Ultimate displacement (estimated for ductile flexural column) = Δ_{bb}

Fig. 3 Estimated performance curves.

6. Conclusions

The following conclusions were obtained from this study:

1. The experimental study of the first series verified that the application of RC columns with wide hoop spacing at mechanical splices had limited negative effects and reduced the shear strength of shear-critical columns by up to 12%.
2. Two structural indices for evaluating the shear strength of columns with the proposed hoop arrangement were presented to consider the reduction in shear strength.
3. The experimental study of the second series confirmed that the application of the proposed hoop arrangement had less negative effects on the seismic performance of ductile-RC columns if the location of rebar jointing was outside of the plastic zone.
4. The proposed shear strength evaluation method had strong applicability to estimate the seismic performance of ductile RC columns with the proposed hoop arrangement.

References

1) Yoshino, T., Kobayashi, K. and Ase, M., (1996). "Intensive shear reinforcing method for PCA Members with Splice sleeve joint." In: 11th WCEE, Paper No. 1209.
2) Sanada, Y., Konishi, D., Khanh, N. and Adachi, T., (2011). "Experimental study on intensive shear reinforcement for RC beams with mechanical couplers." In: Proceedings of fib Symposium PRAGUE, 1, 547-550.
3) Architectural Institute of Japan (AIJ), (1990). "Design guidelines for earthquake resistant reinforced concrete buildings based on ultimate strength concept" [in Japanese].
4) Kowalsky, M. and Priestley, M.J.N., (2000). "Improved analytical model for shear strength of circular reinforced concrete columns in seismic regions." ACI Structural Journal, 97 (3), 388-396.
5) ASCE/SEI 41-06, (2007). "Seismic Rehabilitation of Existing Buildings." American Society of Civil Engineers.
6) Berry, M.P. and Eberhard, M.O., (2005). "Practical performance model for bar buckling." Journal of Structural Engineering, 131(7), 1060-1070.

Collapse Analysis of Ship Hull Girder Using Idealized Structural Unit Method

Han Htoo Htoo Ko
Ship Structural Integrity Subarea, Department of Naval Architecture and Ocean Engineering

Key Words: *Ship Hull Girder Strength, Collapse Analysis, Idealized Structural Unit Method, ISUM plate element*

1. Introduction

In order to predict the collapse behavior of a ship hull girder in waves including the post-collapse behaviors required for a structural risk assessment, a coupled system of motion/collapse analyses of a hull girder was developed in my laboratory. The rigid body motion and hydrodynamics load distribution is calculated by SSODAC (Shell Structure Oriented Dynamic Analysis Code) and the structural collapse behavior by ISUM (Idealized Structural Unit Method).

In this study, after joining the development of the pre/post processor to automate the input data generation between two analysis codes, I performed the collapse analysis of a 5250 TEU containership, and investigated the collapse behavior. Through the process of the analysis, the need for the improvement of ISUM plate element has been noted for modeling some parts of ship structure, so that it has rotational nodal DOFs as well as the translation DOFs. So, as the second part of the study, I developed a new ISUM plate element and examined the applicability through a comparison with the analytical solution of elastic large deflection behavior of a simple plate model.

2. SSODAC/ISUM System

2.1 Collapse analysis of structure

Idealized Structure Unit Method (ISUM) is similar to the traditional Finite Element Method (FEM). Basically, there are two kinds of elements, ISUM beam element and ISUM plate element. The element size of ISUM is larger than those of FEM. One of the main feature is that initial imperfections of the element can be considered in the element modelling.

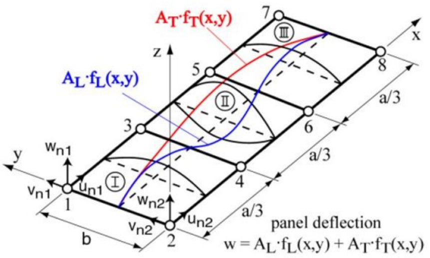

Fig.1 ISUM plate system

Figure 1 shows the ISUM plate element system. A rectangular plate is divided into three ISUM plate elements. The origin of each plate is at the edge of the whole plate panel. Each plate node has 3 translational degree of freedom in x, y and z direction namely u_n, v_n and w_n which means that plate itself does not have bending stiffness. Since the stiffeners are attached to the plate, neglecting the rotational degree of freedom does not have effect on the result and it can also reduce the computational time.

2.2 Wave load analysis

Hydrodynamic scattering are analyzed on Singularity Distribution Method (SDM). Shell Structure Oriented Dynamic Analysis Code (SSODAC) calculates time history of pressure distribution on the hull surface, rigid body motions and resulting inertia force distribution on cargo, ballast water, etc. Linear potential theory is employed in the present study.

2.3 Work flow procedure of system

Figure 2 shows the work flow procedure of the system.

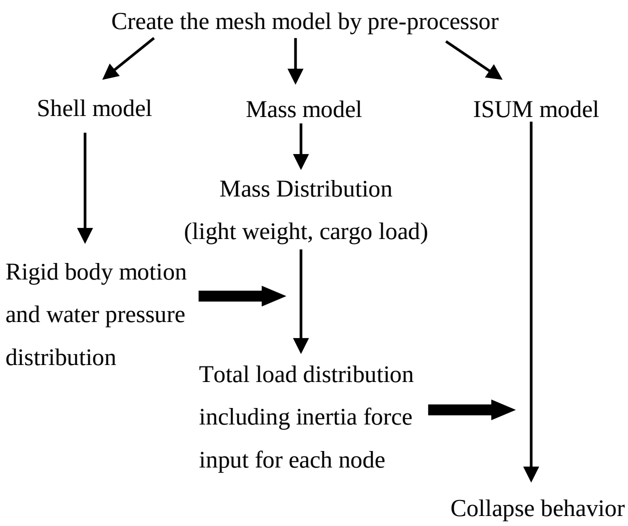

Fig. 2 Work flow procedure

3. Container Ship Analysis

A 5250TEU container ship is used for the analysis. Principal particulars are as shown in the Table 1.

Table 1 Principal particulars of the model for analysis

Length	Breadth	Depth	Draft
267.00 m	39.80 m	23.60 m	12.50 m

The miship part is modelled by the ISUM elements while the others are by the conventional elastic shell elements. Small mesh size is used in the ISUM part, but it is much coaser than that required in the elastoplastic analysis by the conventional shell element. Initial deflection of elements are also assigned.

Wave load of 20 time steps are applied to the model. Head sea condition is used and wavelength is the same as the ship length. Pressure distribution of the hogging mode is shown in Fig. 4.

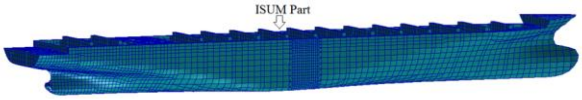

Fig. 3 Container ship model

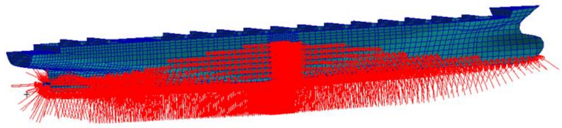

Fig.4 Pressure distribution of hogging condition

3.1 Result of container ship analysis

Global deformation of ship can be seen in Fig. 5 and also half-model deformation is shown in Fig. 6.

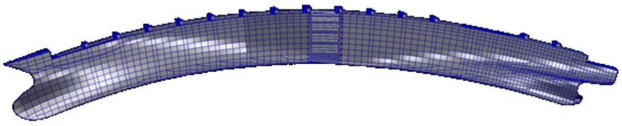

Fig.5 Global deformation of container ship

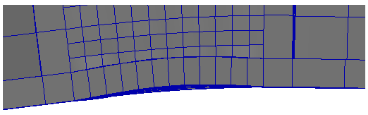

Fig.6 Bottom deformed shape at midship part (half-model)

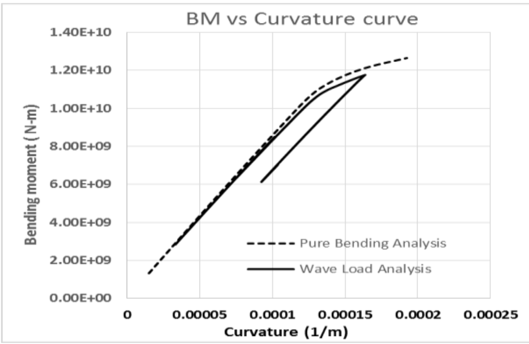

Fig.7 Bending moment and curvature curve

Figure.7 shows the bending moment-curvature curves obtained by the pure bending analysis and the wave load analysis. The latter includes the effect of lateral pressure on the bottom, and hence the bending capacity is slightly smaller than that of the pure bending case.

4. Improved ISUM Element

In order to make it easier to generate the element mesh in the unstiffened part of ship, new ISUM plate element with rotational DOFs is developed. The nodal displacements are interpolated by bilinear function Ni as

$$\begin{Bmatrix} u \\ v \\ w \end{Bmatrix} = \sum_{i=1}^{4} N_i \begin{Bmatrix} u_i \\ v_i \\ w_i \end{Bmatrix} + \sum_{i=1}^{4} z N_i \begin{Bmatrix} \theta_{yi} \\ -\theta_{xi} \\ 0 \end{Bmatrix} \tag{1}$$

Strain increment equation of newly developed element becomes

$$\begin{Bmatrix} \Delta\varepsilon_x \\ \Delta\varepsilon_y \\ \Delta\gamma_{xy} \\ \Delta\gamma_{xz} \\ \Delta\gamma_{yz} \end{Bmatrix} = \begin{Bmatrix} \dfrac{\partial \Delta u}{\partial x} \\ \dfrac{\partial \Delta v}{\partial y} \\ \dfrac{\partial \Delta u}{\partial y} + \dfrac{\partial \Delta v}{\partial y} \\ \dfrac{\partial \Delta u}{\partial y} + \dfrac{\partial \Delta w}{\partial y} \\ \dfrac{\partial \Delta v}{\partial y} + \dfrac{\partial \Delta w}{\partial y} \end{Bmatrix} - \begin{Bmatrix} z\dfrac{\partial^2 \Delta w}{\partial x^2} \\ z\dfrac{\partial^2 \Delta w}{\partial y^2} \\ 2z\dfrac{\partial^2 \Delta w}{\partial x \partial y} \\ 0 \\ 0 \end{Bmatrix} + \begin{Bmatrix} \dfrac{1}{2}\left(\dfrac{\partial \Delta w}{\partial x}\right)^2 \\ \dfrac{1}{2}\left(\dfrac{\partial \Delta w}{\partial y}\right)^2 \\ \dfrac{\partial \Delta w}{\partial x}\dfrac{\partial \Delta w}{\partial y} \\ 0 \\ 0 \end{Bmatrix} \tag{2}$$

where w is the sum of local panel deflection nodal deflection w_L, given by the analytical function of panel collapse mode and the overall deflection given by the nodal displacement, w_n.

4.1 Validation of new ISUM element

In order to validate the new ISUM plate element, as a fundamental case, the elastic deflection behavior of two-edge simply supported plate under longitudinal thrust is analyzed as shown in Fig.8. The corresponding analytical solution is given by

$$w = \frac{a_0}{1 - \sigma / \sigma_{cr}} \tag{3}$$

where σ_{cr} is elastic buckling stress and a_0 is the maximum initial deflection of sinusoidal mode.

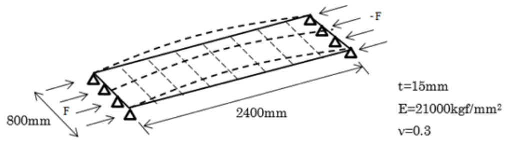

Fig.8 Two edge simply-supported plate under thrust

Comparison between analytical solution and simulation result shows a good agreement as shown in Fig.9.

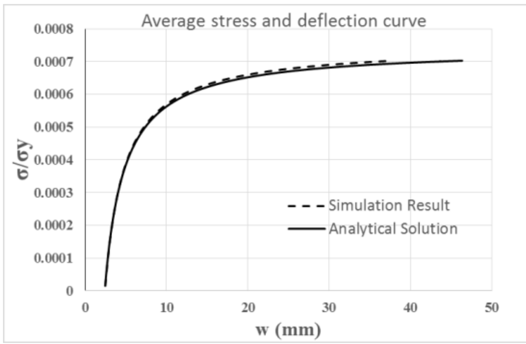

Fig. 9 Average Stress and Deflection Curve

5. Conclusions

1) The ultimate strength was not attained under the maximum wave height of 20m in the present study.
2) New ISUM element gives a good prediction of plate buckling behavior and can be utilized in the unstiffened panel of the ship.

References

Fujikubo, M. and Kaeding, P., 2002, New simplified approach to collapse analysis of stiffened plates, Marine Structures, Vol.15, pp 251-283.

Probabilistic Prediction of Broaching and Broaching-induced Roll for Ships with Twin Propellers and Twin Rudders

Thet Zaw Htet
Ship Design Subarea, Department of Naval Architecture and Ocean Engineering

Key Words: *Calm-water Manoeuvring Coefficients, Broaching-induced roll, Broaching Probability, Tumblehome*

1. Introduction

Accurate prediction of broaching for ships in regular and irregular waves is still a challenge, especially for ships with twin propellers and twin rudders because of the emergence of a propeller and rudder as a result of large rolling due to broaching. As ships having twin propellers and twin rudders, ONR tumblehome topside vessel[1)] and ONR flare topside vessel[2)] were major subject ships. By taking into account the propeller and rudder emergence, agreements between model experiments and the numerical simulation have been significantly improved[1)] for flare vessel but still some disagreement can be found for the ONR tumblehome topside vessel[2)].

Therefore, to predict the probabilities of broaching and broaching-induced roll for a tumblehome vessel and a flare vessel, it is necessary to improve the model for a tumblehome first.

For investigating the previous modeling of ONR tumblehome vessel, an inconsistent approach which considers the nonlinear manoeuvring coefficients but neglects all other higher order terms[2)] was used. However, it is not guaranteed whether this kind of partial consideration of higher order order terms leads to a good result. Therefore, in this study, the simulation model for the tumblehome vessel was attempted to improve by examining a factor in the modeling, i.e. non-linearity of calm-water forces and moments and the effect of this factor was explored with existing and newly executed free-running model experiments.

2. Estimation method for broaching probability

The broaching probability in irregular seas could be estimated by integrating the probability density function of local wave height and local wavelength[3)] within the broaching region obtained by the use of a time-domain simulation model[1)] in regular waves. The simulation model is based on a coupled surge-sway-yaw-roll MMG-type manoeuvring model[4)] with a PD autopilot and wave-induced forces and moments, which are estimated with a linear slender body theory under low encounter wave frequency[5)]. For the amplitude of the wave-induced forces, empirical corrections based on captive tests[6)] were added. Assuming that wave steepness and wave-induced motions except for the roll are small, the interaction between wave and manoeuvring forces are ignored as higher order term. The propeller and rudder emergence[2)] are taken into account. The roll damping coefficients are obtained by conducting roll decay tests.

In both simulations and experiments, broaching, surf-riding and capsizing were judged with a qualitative judging criterion proposed by Umeda and Hashimoto[7)]. The ITTC(1973) spectrum and a wave staticstics for the North Atlantic are used in this work.

3. Comparison with free running model tests

3.1 In regular waves

The numerical simulations were executed by using the above mentioned model with and without nonlinear terms of calm-water manoeuvring coefficients and then compared with the existing free-running model experiments conducted by Hashimoto et al[6)].

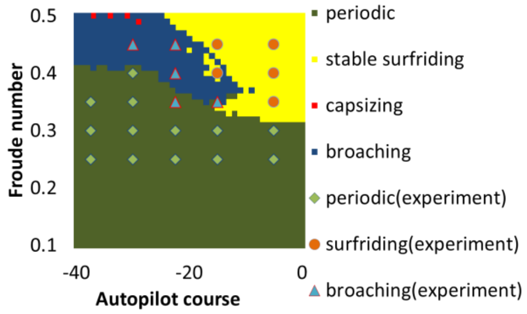

Fig. 1 Comparison between experiments and calculations without nonlinear calm water manoeuvring coefficients for wave steepness of 0.05 and wavelength to ship length ratio of 1.25.

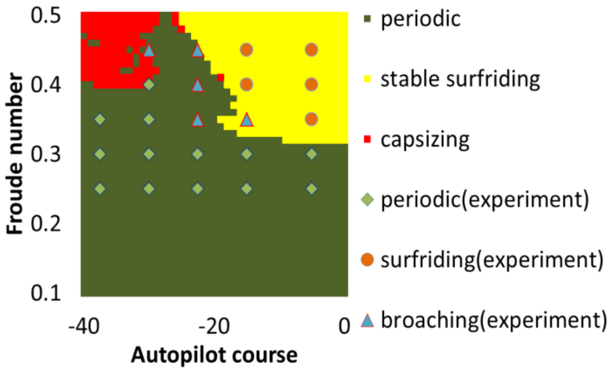

Fig. 2 Comparison between experiments and calculations with nonlinear calm water manoeuvring coefficients for wave steepness of 0.05 and wavelength to ship length ratio of 1.25.

The results shown in Figs. 1-2 indicate that the calculation without nonlinear terms of calm-water manoeuvring forces provides better agreement with the experiments.

The reason of reducing broaching region with nonlinear terms of calm-water manoeuvring forces is that the contribution of these nonlinear manoeuvring coefficients in yaw act in the direction for increasing damping so that broaching could be prevented.

The reason of increasing capsizing region with nonlinear terms of calm-water is that, when the ship is surf-ridden, all of the calm-water manoeuvring nonlinear terms in sway equations of motion could induce an additional moment toward capsizing.

3.2 In irregular waves

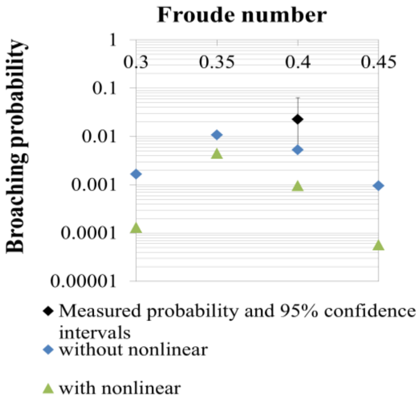

Fig. 3 Comparison in broaching probability in irregular waves between experiments and calculations with and without nonlinear manoeuvring coefficients.

The free-running model experiment in irregular waves was newly conducted and the simulation results with and without nonlinear manoeuvring coefficients were compared with the 95% confidence intervals of experimental result of broaching probability which is 0.02255 as shown in Fig. 3. This indicates the calculation results without nonlinear maneuvering coefficients exist inside the range, whereas the calculation results with nonlinear terms are outside.

The reason of obtaining better results without nonlinear calm-water manoeuvring coefficients can be presumed as follows. The effect of nonlinear terms of calm-water manoeuvring coefficients cannot be denied, but it could be cancelled out by other terms such as higher order terms of wave effects on manoeuvring coefficients, which were not taken into account[8]. As a result, these nonlinear terms of calm-water manoeuvring coefficients could cause additional damping not to result in broaching.

4. Assessment of broaching danger in actual seas

For the assessment of broaching danger in actual seas, a comparison study of probabilistic prediction of broaching and broaching-induced roll, which is larger than 50 degrees, are done for the ONR tumblehome and flare vessels. Here, the probabilities for both vessels are calculated without nonlinear calm-water manoeuvring coefficients.

As shown in Fig. 4, the broaching probability of the flare vessel is larger than that of tumblehome for the Froude number of 0.35 or over as the same with we observed in the experiments. Here, the reason why broaching probability decreases for Fn=0.4 and 0.45 for the tumblehome and for Fn=0.45 for the flare is that, the ship speed is higher than the critical speed for broaching so that the ship could escape from the broaching.

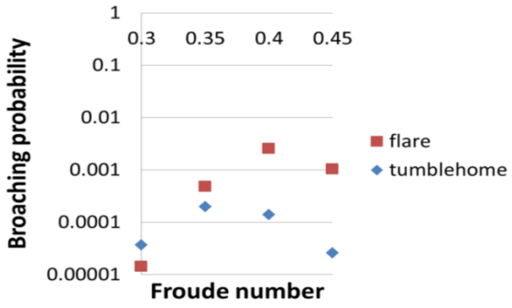

Fig. 4 Broaching probability in the North Atlantic.

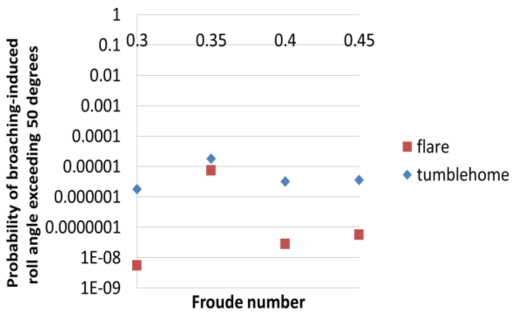

Fig. 5 Probability of broaching-induced roll angle exceeding 50 degrees in the North Atlantic.

As shown in Fig. 5, for the probability of roll angle exceeding 50 degrees, the probability of the tumblehome vessel is much higher than that of flare because of the smaller righting arm due to its shape[6].

5. Conclusions

For the ONR tumblehome topside vessel, the simulation without nonlinear terms of calm-water manoeuvring forces provides better agreements with the free-running model experiments in regular and irregular waves than that with nonlinear terms.

Although the broaching probability of the tumblehome is smaller than that of the flare, the tumblehome is more dangerous because of its higher probability of broaching-induced roll angle exceeding 50 degrees.

References

1) Umeda N, Usada S et al: (2016) JMST, 21:23-27.
2) Umeda N, Furukawa T et al: (2014) Proceedings of 30th ONR Symposium on Naval Hydrodynamics, Hobart, USB disk.
3) Longuet-Higgins MS: (1983) Proceedings of the Royal Society of London, Series A389:241-258.
4) Hirano, M: (1980) J Soc Nav Arch Jpn, 147:144-153.
5) Umeda N et al: (1995) Proceedings of the International Symposium on Ship Safety in a Seaway, 14.1-18.
6) Hashimoto H et al: (2011) JMST 16:448-461.
7) Umeda N, Hashimoto H: (2002) JMST 6:111-121.
8) Araki M et al: (2012) J of JASNAOE, 14:85-96.

Study on Sediment Transport around Lampulo Fishing Port on Banda Aceh Coast

Muhajjir
Land Development and Management Area Laboratory, Department of Civil Engineering

Key Words: *Port, field study, sediment transport, morphological changes*

1. Introduction

Lampulo Ocean Fishing Port (PPS Lampulo) with the area of 50 ha is located on the coast of Banda Aceh, Indonesia. The fishing port was built since 2006 and the development will be advanced to gradually until 2030[1]. During the developing phase of the port in the coastal zone, it is necessary to comprehend the potential risk of sedimentation and erosion. This is related to the projected dredging interval and volume of the basin. The development of Lampulo Port will cause the significant impact on coastal morphology. In addition, the presence of estuary Kr. Aceh next to the Port added the issues of sedimentation and erosion due to tidal currents and waves. This is certainly a serious problem that needs to be considered so that the sustainable development of this port can run optimally without causing a significant effect on the environment. Considering the issues, the main purpose of this research is to investigate the on morphology changes of the bed sea profile and the shoreline change due to the port construction.

2. Methodology

2.1 Field Measurement

Field measurement (Fig.1) was carried out for 15 days from August 22nd, 2015 by setting measuring equipment at the location: 755965E and 617600N with the water depth of 4.2 m. The measurement consisted of water level, pressure, current, bathymetry, and sediment sampling. In addition, historical wind data (1999-2009) gained by BMKG Aceh were also considered as primary data. Some of those data were used to support simulation model and partly used to validate the model itself.

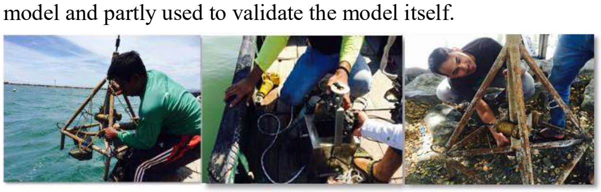

Fig.1 Field measurement activities

2.1 Delft3D Simulation Model

Delft3D is an open source windows-based program used for modeling the change of coastal morphology. In order to complete the field study, the model simulation was performed by coupling of Delft3D-FLOW and Delft3D-WAVE systems. The simulation was carried out for three scenarios which corresponded to West, Northwest and North wave direction for 2 year simulation. The data gained from the field were used in Delft3D numerical program as follows: 1) topography, 2) wind, 3) bathymetry, 4) tidal, 5) current, 6) wave, 7) sediment.

3. Results of Field Measurement

a. Wind data

Wind data were used for wave forecasting in this study. The wind from that the South East and West directions were dominant with distribution of 29.18 % and 25.3 % respectively. However in the wave forecasting, three cardinal directions were used: West, North West, and North, in which the wind blew from the ocean. Wave forecasting was calculated by using the Eq. (1) proposed by the US Army Corps of Engineer[2]. Wave forecast showed that the average of significant wave height and period for West, North West and North were (0.26 m: 2.2s), (0.21m: 1.9s) and (0.18:1.8s) respectively. Results of wave forecasting are shown in Fig.2

$$\frac{gH_s}{U_A^{\,2}} = 0{,}283\tanh\left[0{,}530\left(\frac{gh}{U_A^{\,2}}\right)^{3/4}\right]\tanh\left[\frac{0{,}00565\left(\frac{gF}{U_A^{\,2}}\right)^{1/2}}{\tanh\left[0{,}530\left(\frac{gh}{U_A^{\,2}}\right)^{3/4}\right]}\right] \quad (1)$$

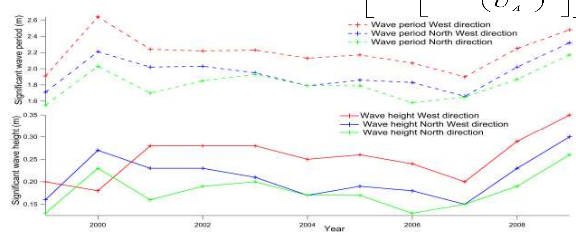

Fig.2 Significant wave height and period yearly by forecating

b. Tide

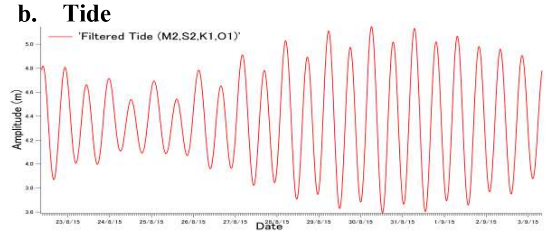

Fig.3 Tidal data of field measurement

As the result of the tidal analysis, the high tide occurred 2 times a day. This showed that the semi-diurnal components M2 and S2 which were influenced by the moon was more dominant than the diurnal components K1 and O1 influenced by the sun. MSL (mean sea level) obtained from the measurement was 4.35 m, HHWL (highest high water level) = 5.30 m, and LLWL (Lowest low water level) = 3.58m.

c. Wave

Fig.4 shows the wave condition on the field. Large values of wave period indicate that the wave at the location was relatively long waves, whereas the wave period given by wave forecasting was short. In term of the wave height, it could be seen that the wave height during measurement period was small.

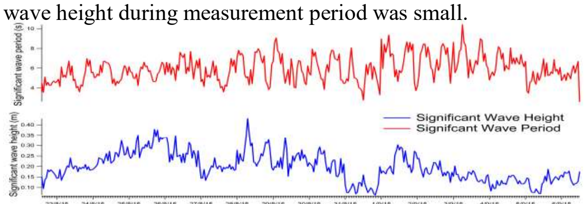

Fig.4 Significant wave height and period by measurement

This is supported by the wave forecasting results shown in Fig.2 which indicated the wave condition at Lampulo waters was calm. This sea was calm because reduction of energy from West direction due to existence of four islands on West side (*close sea*) as shown in Fig. 5(a) and the fetch length of Northwest and North were large (*duration limited*) as shown in Fig. 5(b)

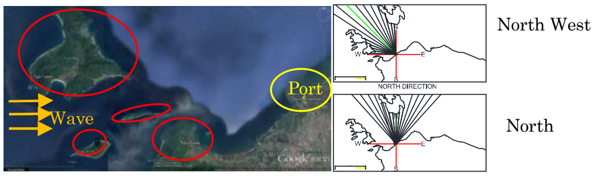

(a) (b)

Fig.5 Wave barrier (a) Fetch length of North West and North wave direction (b)

d. Comparison between wave forecasting and wave measurement

In order to prove wave forecasting result in the previous section, the forecasted and the measured result were compared. Wave height and period have correlation to wind speed as shown in Fig. 6. However, the wave height and period measured are scattered disproportionately to the wind speed data. It indicated that the waves at Lampulo waters were not generated locally, but the generated far in the ocean. Further, the ocean waves propagated and generated variants in wave height and wave period toward shallow waters. In conclusion, instead of inaccurate wave forecasting, the measured data were used as input data for simulation model. The wave data used in simulation model were the waves generated by West, Northwest and North.

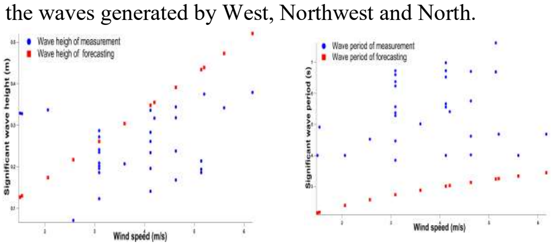

Fig.6 The comparison between wave and wind data

e. Current

Comparison of waves, current and tide were done to determine the factor having greater influence on current formation. As shown in Fig.7, the wave pattern showed nice correlation to the current pattern. It was signed by the increasing and decreasing of both wave and current simultaneously. On the other hand the tide did not contribute dominantly to fluctuation of the current. It was showed by fluctuation of current which was not followed by the fluctuation of the tide.

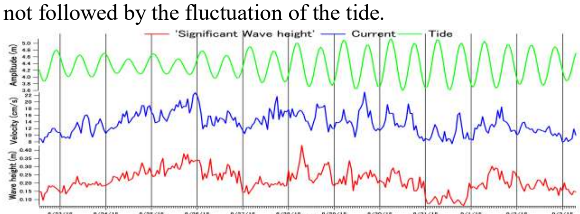

Fig.7 The comparison of wave, current and tide data

4. Validation

Validation of the model was first done by comparing the value and pattern of water level generated by the tide between model and field.

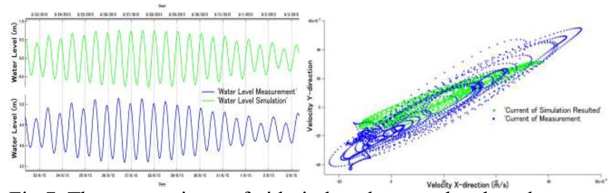

Fig.7 The comparison of tide-induced water level and current between the model and the field measurement

The second validation was carried out by comparing the magnitude and heading of the current. The current data used to validate was only influenced by tide. The result showed that the values, pattern and heading current predicted by the model was close enough to the real current on the field (See Fig. 7). Thus the simulation was conducted reasonably.

5. Result of Simulation

Result of simulation showed the change in morphology of seabed at the points as shown in Fig.6 (a). The changes at Point-B and Point-D indicated erosion with the depth of 0.4 m and 1.5 m respectively. The Point-C experienced a fairly small sedimentation of 1.6 x 10^{-4} m. Point-A and Point-Device Placement water depth did not change at all. Furthermore, total erosion and sedimentation of domain were 786132.18 m^3 and 2351864.71 m^3 respectively. The difference between them was -1564992.84 m^3. As a result, the phenomenon of sedimentation dominated during two years of simulation. It was confirmed by previous research[3)]

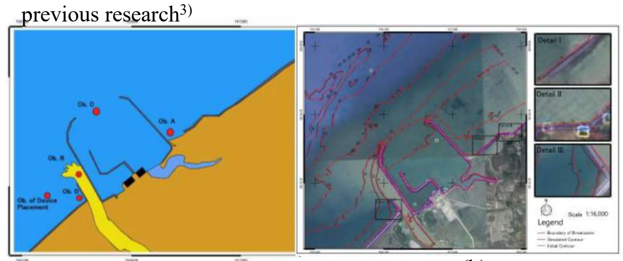

(a) (b)

Fig.6 Observation point of simulation (a) and shoreline change (b)

In addition, shoreline change due to sedimentation and erosion was occurred in three main parts as shown in Fig. 6 (b). Detail I and II in the figure were marked by shoreline advance of approximately 8 m and 9 m respectively, while Details III informed shoreline retreat of 6 m.

6. Conclusion

1. The waves at Lampulo waters were calm, it is due to the wave barrier on the West side of the port and small wind speed. Additionally the current was dominantly influenced by the waves.
2. The wave forecasting was not useful to apply in the simulation, because it was uncorrelated with the measured waves.
3. The presence of Lampulo Fishing Port influences the morphology change such as shoreline and bed sea profile.

7. References

1. DKP Aceh. 2012. *Fisheries Data Statistics of Aceh. 2012*. DKP Aceh: Banda Aceh. [In Indonesian]
2. SPM. 1984. *Shore Protection Manual*. Vol.1,4thed. Washington, D.C.: U.S. Army Engineer Waterways Experiment Station.
3. Rasyif, TM. 2012. *Numerical Simulation: The Influences of Tidal Current Against potential of Sedimentation and Erosion Adjacent Estuary of Kr. Aceh*. Thesis Syiah Kuala University : Banda Aceh [In Indonesian]

Wave-Induced Steady Forces and Seakeeping Performance of an Advancing Ship in Oblique Seas

Ardhana Wicaksono
Ocean Space Development Subarea, Department of Naval Architecture and Ocean Engineering

Key Words: *Steady horizontal forces, steady yaw moment, oblique waves, Kochin function, enhanced unified theory.*

1. Introduction

A ship sailing in natural sea will experience a series of motions which brings into play first- and second-order forces and moments. Added resistance, steady sway force, and yaw moment, are known to significantly influence the overall ship performance. Early development of theoretical analysis was provided by Maruo[1] and Newman[2] for the drift force in the horizontal plane and yaw moment. Kashiwagi[3] proposed another analysis method for the yaw-moment formula at forward speed. Later, Kashiwagi[4] proposed the Enhanced Unified Theory (EUT) taking account of bow-wave diffraction by including n_1-term in the body boundary condition, which improved the estimation of the added resistance. In this paper, wave-induced motions, steady forces and yaw moment, and forward-speed effect are inspected with emphasis on oblique waves by means of New Strip Method (NSM) and EUT.

2. Calculation Method

2.1 Formulation

Let us consider a ship advancing at forward speed U into a plane progressive wave of amplitude A, circular frequency ω_0 and wavenumber k_0 as shown in Fig. 1. Due to the incident waves with angle χ, the ship experiences motions about its mean position with encounter frequency ω. By linear justification, the velocity potential can then be defined as

$$\Phi_T(\mathrm{x,y,z,t}) = U[\Phi_D(x,y,z) + \phi_s(x,y,z)] + \Phi(x,y,z,t) \quad (1)$$

Here Φ_T, Φ_D, and ϕ_s denote the velocity potentials of the total flow, steady basis flow, and steady disturbance, respectively. To obtain the unsteady velocity potential Φ, the EUT is applied as derived in upcoming sections.

2.2 Wave-Induced Steady Forces and Moment

After solving boundary-value problems for the unsteady velocity potentials, the second-order wave-making steady forces and moment can be computed with formulas in Kashiwagi[3]:

$$\frac{R}{\rho g A^2} = \frac{1}{4\pi k_0}\left[-\int_{-\infty}^{k_1} + \int_{k_2}^{k_3} + \int_{k_4}^{\infty}\right] \{|C(k)|^2 + |S(k)|^2\}\frac{\kappa(k-k_0\cos\chi)}{\sqrt{\kappa^2-k^2}}dk \quad (2)$$

$$\frac{F_y}{\rho g A^2} = -\frac{1}{4\pi k_0}\left[-\int_{-\infty}^{k_1} + \int_{k_2}^{k_3} + \int_{k_4}^{\infty}\right]\Im\{2C(k)S^*(k)\}\kappa dk + \frac{\sin\chi}{4\pi}\left[-\int_{-\infty}^{k_1} + \int_{k_2}^{k_3} + \int_{k_4}^{\infty}\right]\{|C(k)|^2 + |S(k)|^2\}\frac{\kappa}{\sqrt{\kappa^2-k^2}}dk \quad (3)$$

$$\frac{M_z}{\rho g A^2} = -\frac{1}{4\pi k_0}\left[-\int_{-\infty}^{k_1} + \int_{k_2}^{k_3} + \int_{k_4}^{\infty}\right]\Re\{C'(k)S^*(k) \; C^*(k)S'(k)\}\kappa dk - \frac{1}{2}\sin\chi\Re[C'(k_0,\chi) + iS'(k_0,\chi) + \frac{1}{k_0}\left(\tau + \frac{k_0\cos\chi}{K_0}\right)H(k_0,\chi)] \quad (4)$$

with τ and κ being the Hanaoka's parameter and 3D wave number, respectively. k_1 to k_4 are the k-waves system that represents the wave pattern around the hull.

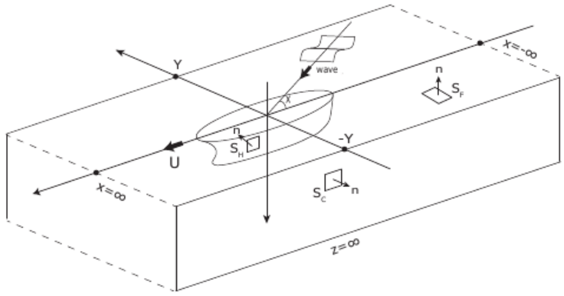

Fig. 1 Coordinate system and notations.

2.3 Enhanced Unified Theory and Kochin Function

The wave amplitude functions $C(k)$ and $S(k)$ in (2) to (4), are defined as symmetric and antisymmetric components of ship-generated progressive waves, respectively, with respect to the ship's y-center plane. As the symmetric component can be expressed as

$$C(k) = C_7(k) - \frac{\omega\omega_0}{g}\sum_{j=1,3,5}\frac{X_j}{A}C_j(k) \quad (5)$$

Based on EUT, $C_j(k)$ can be computed by

$$C_j(k) = \int_L Q_j(x)e^{ikx}dx \quad (6)$$

$Q_j(x)$ represent the x-axis linear source strength ($z=0$ on the free surface) in the outer solution. This is then determined as a solution of integral equation to be attained through matching between inner and outer solutions, that can be written as

$$Q_j(x) + \frac{i}{2\pi}\left(1-\frac{\sigma_3}{\sigma_3^*}\right)\int_L Q_j(\xi)f(x-\xi)d\xi = \sigma_j(x) + \frac{U}{i\omega}\hat{\sigma}_j(x) \quad (7)$$

$$Q_7(x) + \frac{i}{\pi}\sigma_7\left\{Q_7(x)h_1(\chi) - \int_L Q_7(\xi)f(x-\xi)d\xi\right\} = \sigma_7 e^{ilx} \quad (8)$$

$$h_1(\chi) = \csc(\chi)\cosh^{-1}(|\sec\chi|) - \ln(2|\sec\chi|) \quad (9)$$

in respect to the radiation and diffraction. $f(x-\xi)$ include 3D and forward-speed effects. $\sigma_j(x)$ and $\hat{\sigma}_j(x)$ denotes 2D Kochin functions from the particular solution of the inner problem.

The inner solution can be given in the form

$$\phi_j(x;y,z) = \varphi_j(y,z) + \frac{U}{i\omega}\hat{\varphi}_j(y,z) + C_j(x)\{\varphi_3(y,z) - \varphi_3^*(y,z)\} \quad (10)$$

$$\phi_7(x;y,z) = -e^{-k_0z+ilz}\cos(k_0 y\sin\chi) + C_7(x)\{\psi_{2D}(y,z) + e^{-k_0z+ilz}\cos(k_0 y\sin\chi)\}e^{ilx} \quad (11)$$

The first line on the right-hand side of (10) and (11) represents the particular solution and the second depicts homogenous solution. Also, ψ_{2D} is solved to retain the contribution of n_1-term to approximate the bow wave diffraction in the longitudinal direction.

3. Ship Model and Experiment

The ship in concern is a bulk carrier named JASNAOE-BC084, 320 m long, 58 m wide, and 20.8 m deep, with $CB = 0.84$. Her cross sections are projected to the length as in Fig. 2.

The experiment was done in the tank of Mitsubishi Heavy Industries. Measurement was done at $Fn = 0.00\sim0.1239$ in $\chi = 30°\sim180°$, with $\lambda/L = 0.4\sim1.5$. Incident waves were recorded by two methods: near-field (ENC) and far-field (STN), by probes installed on the carriage and on tank's sides, respectively.

4. Computed and Measured Steady Forces

Forces and moment at $Fn = 0.0367$ are shown in Fig. 3. The agreement is observed to be fairly good with some issues.

In oblique waves for a real ship, symmetric and antisymmetric waves component are incorporated simultaneously to the results. This is indicated by coupling of hydrodynamic forces, its corresponding motions, and resulting wave amplitude functions that are fundamental in a prediction of steady forces and moment.

At certain λ/L, the wave amplitudes recorded by far- and near-field probes vary significantly. This trend is remarkable when the incident waves are disturbed by significant ship-generated steady and unsteady waves which are dominant in certain wave conditions. As an example at $Fn = 0.1239$, on the added resistance in moderate speed, the STN recorded notably smaller incident wave amplitudes than the ENC which is proportional to larger nondimensionalized R values measured by STN. The far-field probes measured the incident waves affected by dissipated waves.

5. Effect of Forward Speed to the Steady Forces

The forward speed dependence is inspected on three representative λ/Ls equal to 0.6, 1.0, 1.5. For example, the yaw moment case in $\lambda/L = 1.0$ is shown in Fig. 4. Along with the speed rise, Doppler effect will take place, τ shift to the longer λ/L, that cause a drastic change of wave pattern around the hull.

6. Discussions and Conclusions

The findings in this study may be summarized as follows:

- EUT solutions are inspected to predict the steady horizontal forces and yaw moment better than NSM to a certain extent.
- In shorter waves, steady forces have been observed to increases along with the speed, then reach a certain value, and became constant. Diffraction part is dominant and is strongly correlated to ship ends' geometry in the computation. Therefore, rigorous evaluation of source strength on a real-shaped ship is crucial.
- From λ/L≈1.0 to the long waves, steady forces are mainly contributed by the radiation Kochin functions that are fairly sensitive to the speed. In oblique waves, an improvement on the estimation of hydrodynamic forces and motions is required.
- Employment of two methods in measuring the incident wave amplitudes is beneficial in the physical understanding of ship-wave interaction problem.

References

1) Maruo, H.: Bull of Fac of Eng, YNU, pp.73-91, 1960.
2) Newman, J.N.: JSR, Vol.11, No.1, pp 51-60, 1967.
3) Kashiwagi, M.: Schiffstechnik, Vol.39, No.1, pp 3-16, 1992.
4) Kashiwagi, M.: Trans of WJSNA, No.89, pp 77-89, 1995.

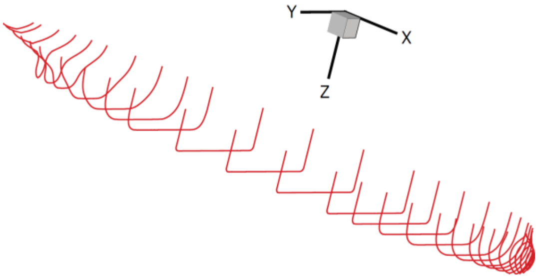

Fig. 2 Body plan of JASNAOE-BC084.

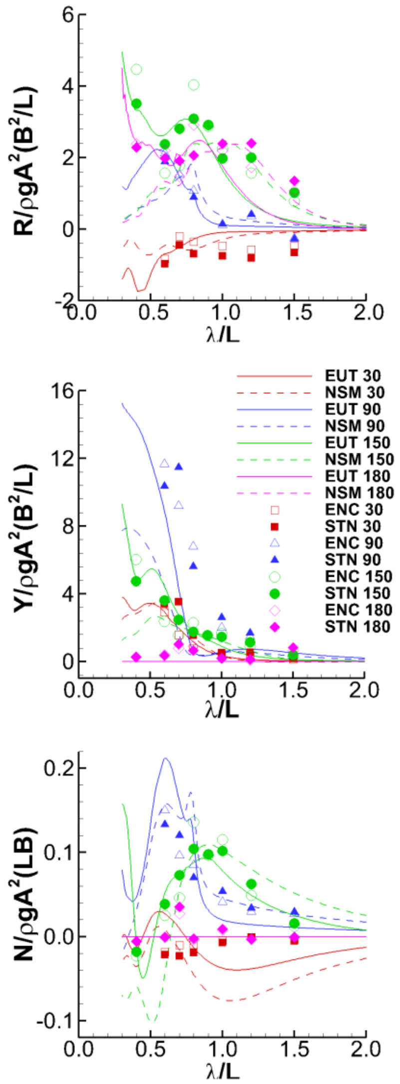

Fig. 3 R_{AW}, Y_{AW}, N_{AW} at $Fn = 0.0367$.

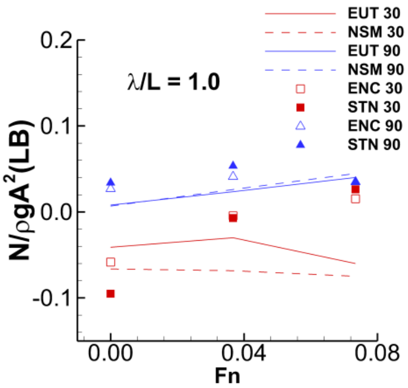

Fig. 4 Forward-speed dependence of N_{AW} at λ/L =1.0.

The EFD and CFD Study of the Bulbous Rudder with Asymmetric Horizontal Fins with Different Angles of Attack in Ship and Propeller Wake Field of KVLVV2 Tanker

Truong Quang Tho
Hull Form Design Sub-Area, Department of Naval Architecture and Ocean Engineering

Key Words: *Energy-Saving devices (ESDs), Rudder-Bulb-Fin system (RBFS), Computational Fluid Dynamic (CFD), EFD, calm-water*

1. Introduction

With the recent rapid price increase of fuel as well as the fuel shortage and the greenhouse effect has escalated rapidly. In the shipbuilding industry and the operating will also not be an exception. In order to solve those problems, many Energy-Saving devices (ESDs) have been designed and installed on the ship in general as well as around propeller in particular. One of those solutions is the Rudder-Bulb-Fin system (RBFS) which is an ESD installed on a rudder. The horizontal fins on the both sides of rudder bulb share the same foil section, but the suction side faces are different. With the recent growth of Computational Fluid Dynamic (CFD), CFD has been chosen to become the suitable method to solve in this project. The rudder bulb can reduce the propeller hub vortex and the fins produce thrusts in the rotational flows generated by the propeller. The installation angle of fin around -2 to 1 degree with 1-degree increment for the fins on the both sides have been done to find out the best energy effect fin. Validating the results by comparing with experiment result is an absolute necessary. Thus, the experiment was conducted at towing tank of Osaka University (EFD) using KVLCC2 ship model for zero degree of fin installation angle.

2. Methods

The objective ship is the KRISO Very Larger Crude Carrier which called KVLCC2, working at full scale speed 15.5 knots. The length between forward and aft perpendicular is 3.2 meters. Ship beam, draft and displacement are 0.5 (m), 0.208 (m) and 0.313 (m^3), respectively. The longitudinal center of buoyancy is located in front of mid-ship 3.48% of ship length. The experiment was carried out in the towing tank of Osaka University with fully loaded condition at Froude number equals to 0.142 corresponding to model speed 0.795 m/s and Reynold number equals 2.05e6 corresponding to the 3.2m long ship model.

CFDSHIP-IOWA version 4.5 is used for numerical prediction in present research. It is an incompressible URANS/DES solver designed for ship hydrodynamics. The momentum equations were solved with the body force distribution representing propeller effect as the source terms. The computational domain extends from $-0.5<x/L<2.35$, $-1<y/L<1$ and $-1<z/L<0.22$, where L is ship length. For inlet boundary condition, the free stream inflow velocity is set as non-dimensional ship speed ($u/U_0=1$). The exit boundary condition is used for the outlet. The far field boundary conditions are implemented on the domain top and bottom. Zero gradient boundary condition is implemented on the domain sides. No-slip boundary condition is applied for all the solid surfaces. A slip boundary condition with $u/U_0=0$ and (v/U_0 and w/U_0) based on propeller angular velocity; $2\pi r_{hub} n$ is imposed on the hub surface, r_{hub} is the radius at the grid point on the hub surface and n is the propeller revolution rate.

3. Results

3.1 Flow field analysis

In figure 1, the flow field is extracted from the section at the AP position (x/L=1) across the rudder surface. We can see from the figure that the hub vortex would tend to move to the left side. The vortices are truncated by the fins in, the starboard side, especially. The hub vortex location is lowered due to the fin and bulb. The hub vortex area is smaller and axial velocity in its core decreases.

Figure 2 plots the axial velocity contours limited to $u/U_0=1.1$ along several x/L sections across the portside and starboard side fin. The tip vortex is observed clear on the portside fin. It indicates the positive pressure difference between upper and lower surface is pushing the fin upward. The fluid flows across from pressure side to suction side indicating a lift loss. The hub vortex is mainly attached under the starboard of bulb surface. On the other hand, a larger area of flow separation under the starboard fin (pressure side) near the root appears. The tip vortex is relatively smaller compared with the portside one. It implied the larger drag on the fin. Thus, this ESD (0-degree angle of attack) configuration is not an optimal design, especially for the starboard side fin. It is necessary to understand the flow angle of attack into the fin.

3.2 Self-propulsion factors

The self-propulsion factors would be validated against measured data in Table 1. There is a comparison between the normal rudder and rudder-fin case. With the appearance of a bulb and fins on the rudder, thrust deduction increases around 2%, wake factor decreases 2% in simulation and 5% in experiment; hence the hull efficiency increases 4% in simulation and 7% in experiment.

The total resistance with the propeller for different angles of attack is illustrated in Table 2. Besides that, the total resistance without propeller also was found out in order to estimate the self-propulsion factors. The lowest resistance R=5.6508 shows the best angle of attack; zero degree for portside and -1 degree for starboard side. By comparing with R=5.784 of normal rudder, the total resistance is reduced about 2.3% by the best angle of attack and 1.8% by zero angle of attack.

The self-propulsion factors in Table 3 also indicate the same best angle of attack. The thrust deduction (1-t) increases around 3% comparing with zero angle of attack case and 4.9% comparing with normal rudder case.

Table 1 Self-propulsion factors

	1-t	1-w	η_H
CFD-Normal	0.7643	0.4601	1.6612
CFD- Fin	0.7797	0.4527	1.722
EFD-Normal	0.7788	0.4468	1.7431
EFD-Fin	0.7953	0.4251	1.8710

Table 2 Total resistance for different angles of attack

Resistance R[N]		Angle of Attack (deg.) [portside]			
		-2	-1	0	1
Angle of Attack (deg.) [starboard side]	-2	5.6628	5.6539	5.6599	5.6611
	-1	5.7091	5.7085	5.6508	5.6593
	0	5.6632	5.6655	5.6807	5.7164
	1	5.7220	5.6712	5.7246	5.6701

Table 3 Self-propulsion factors for different angles of attack

Self-propulsion factors			Angle of Attack (deg.) [portside]			
			-2	-1	0	1
Angle of Attack (deg.) [starboard side]	1-t	-2	0.7909	0.8035	0.7912	0.8012
		-1	0.7905	0.7936	0.8037	0.7836
		0	0.7944	0.8021	0.7797	0.7881
		1	0.7768	0.8022	0.7909	0.8030
	1-w	-2	0.4531	0.4483	0.4532	0.4533
		-1	0.4529	0.4487	0.4483	0.4533
		0	0.4483	0.4483	0.4527	0.4536
		1	0.4535	0.4483	0.4536	0.4530
	η_H	-2	1.7454	1.7921	1.7459	1.7674
		-1	1.7453	1.7685	1.7925	1.7288
		0	1.7718	1.7894	1.7222	1.7373
		1	1.7130	1.7895	1.7437	1.7726

4. Conclusions

This research concentrated on the different benefits among the angles of attack which adjusted from -2 to 1 degree with 1-degree increment for both sides. The best angle of attack has been found. The rudder-fin-bulb system shows the lower resistance and better self-propulsion factors than the normal rudder. The numerical results including rudder flow field and self-propulsion factors had been validated by experimental data for the fins with zero angle of attack firstly. The larger flow separations were found out near the root while the smaller flow separations near the tip. On the contrary for the best angle of attack; zero degree for portside and -1 degree for starboard side; very small flow separation near the root, however, the flow separation near the tip becomes larger. By this point, the plan for the future is beginning to take shape in the researcher's mind.

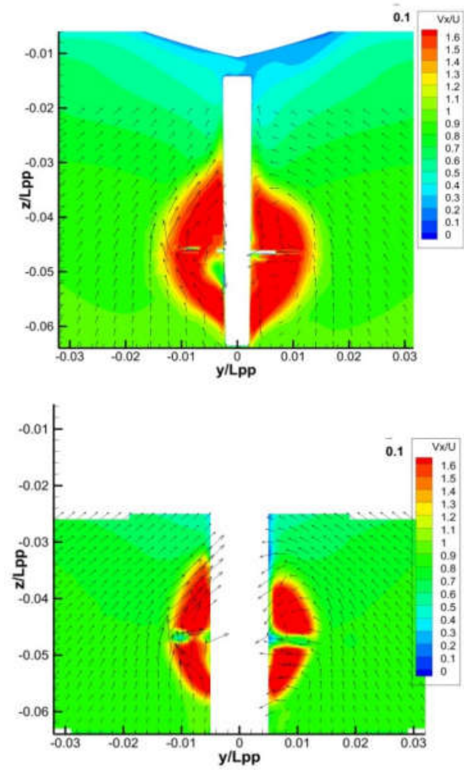

(a)

(b)

Fig. 1 Axial velocity profiles and cross flow vectors at x/L=1 for rudder-fin simulation (a) and experiment (b)

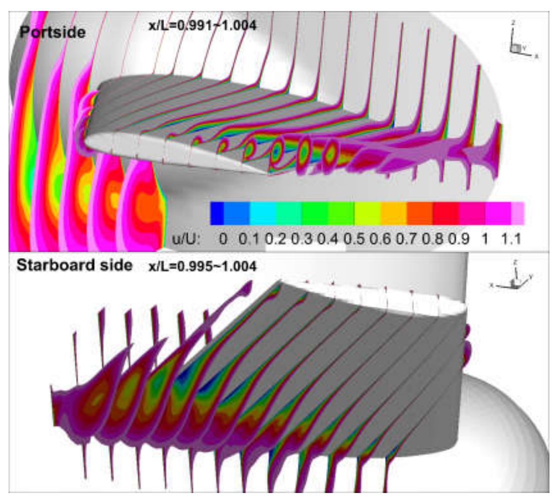

Fig. 2 Velocity sections along fin chord-wise direction

References

1) Kim, JH, Choi, JE, Choi, BJ, and Chung, SH (2014). "Twisted Rudder for Reducing Fuel-Oil Consumption," Int J Nav Archit and Ocean Eng, Vol 6, pp 715-722.
2) Choi, YB (2008) "Energy Saving Devices," SNAME Tech Section 2008-2009, Greece.
3) Kaoru Aoyagi,B.S. thesis, Osaka University.

A Study on Influence of the Difference in Heading Models on Fatigue Assessment Results

Luis De Gracia
Ocean Material Engineering Subarea, Department of Naval Architecture and Ocean Engineering

Key Words: *fatigue, crack propagation, storm model, wave direction, crack propagation retardation.*

1. Introduction

In order to improve the preciseness of ship's fatigue assessment, fatigue crack propagation (FCP) analysis has been proposed as a rational approach for fatigue assessment of ship structure member. The crack propagation behavior strongly depends on the load sequence. The accuracy of fatigue crack propagation analysis depends on the emulation capability of real load sequence. Nowadays, wave models based on various sources of wave data (satellite measurement, hindcast and onboard measurement) are available and can be used to simulate wave load history.

Tomita[1),2),3)] proposed 'storm model' which can simulate the wave load sequence experienced by ocean-going ships. Kawabe[4)] and Prasetyo[5),6)] modified Tomita's model so that storm waveforms were given by significant wave height sequence and the variation of storm duration can be taken into account. In this conventional storm models, 'all headings model' was adopted in sea keeping analyses. In order to fully examine the effectiveness of the conventional storm models, a comparative study on fatigue assessment results which takes into account the relative heading angle's occurrence probability is necessary.

In this study, SN and FCP based fatigue assessments of the welded joint in a container ship which sails on North Atlantic route are performed. Two routes with large and small heading angle variations are assumed. The occurrence probability distribution of wave direction is determined by using JWA hindcast data. Stress sequences are generated by Prasetyo's storm model. Analyses wherein the variation in wave direction's occurrence probability is considered ('real headings model') or not ('all-headings model') are performed. FCP analyses are performed considering plasticity-induced crack closure by using FASTRAN-II. Fatigue crack propagation lives and characteristics of crack propagation retardation due to excessive loads are compared. Based on these results, the influence of the difference in load sequence model on FCP-based fatigue assessment result is discussed.

2. Wave Model

Let θ, α and χ be the wave direction, ship's heading angle and relative heading angle. In conventional ship's fatigue assessment, the stress response is calculated by using 'all headings model' in which χ is given by a uniform random number. This simplification might deteriorate the preciseness of fatigue assessment. The χ's occurrence probability, f_χ, can be calculated from θ's occurrence probability, f_θ, which can be determined from the hindcast data. f_θ's examples are shown in Fig. 1. North Atlantic Ocean is divided into three zones: North side (NS), Mid side (MS) and South side (SS), and f_θ is determined for each zone. In Fig. 1 it is shown that the prevailing θ ranges from 240º to 360º. Also shown is that the θ's variation in the north side is small compare to that in the south side.

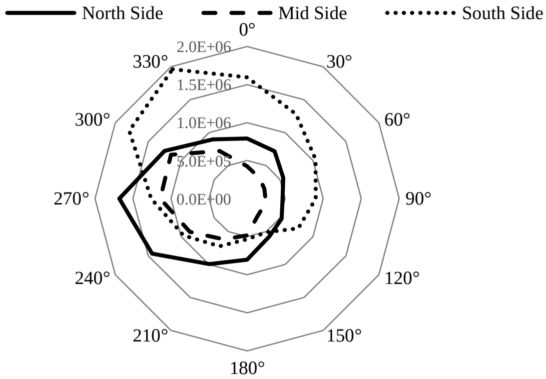

Fig. 1. Wave occurrence probability distribution, f_θ, obtained by hind cast data in the North Atlantic Ocean.

3. Stress Response

3.1 Relative heading angle sequence

Let T_S be the mean wave period. Sequences of (α, H_s, T_S) are generated for the given ship's voyage history by using Prasetyo's storm model[5)]. θ is determined by random number selection with f_θ determined in the previous chapter, and χ is calculated by Eq. (1) at each time.

$$\chi = \alpha - \theta \tag{1}$$

f_χ can be determined by analyzing the generated χ sequence. Let $f_{\chi,AH}$ be f_χ derived from all heading model, and $f_{\chi,RH}$ be that derived from the hindcast's wave direction data.

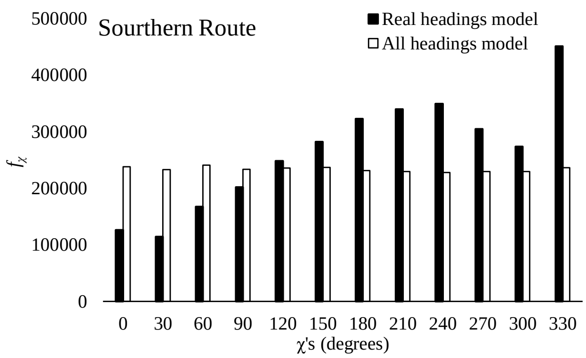

Fig. 2. Relative heading angle experienced in the southern route.

In Fig. 2 it is shown that $f_{\chi,AH}$ is nearly uniform while $f_{\chi,RH}$ shows large variation. The frequency shows gradually changes in the southern route. This is due to the large variance in the ship's heading angle in this route.

3.2 Target structure and stress response

Fatigue assessment of the welded joint in the longitudinal stiffener on the upper deck of the 2800 TEU container ship is performed. Let ΔS denotes the hotspot stress range. ΔS sequence is generated assuming that h_S obeys Rayleigh distribution. The R parameter is determined by using ISSC's wave spectrum. (H_S, T_S, χ) sequences are generated by using all and real headings model. Let $P_{EX,AH}$ (ΔS) and $P_{EX,RH}$ (ΔS) be ΔS's probability of exceedance for the cases of all headings and real headings model. Fig. 3 shows a comparison of $P_{EX,AH}$ (ΔS) and $P_{EX,RH}$ (ΔS) for the southern route. It is shown that the difference in P_{EX} (ΔS) is encountered when the wave directivity is neglected for the southern route. This leads to the small difference in the SN-based fatigue damage analysis results.

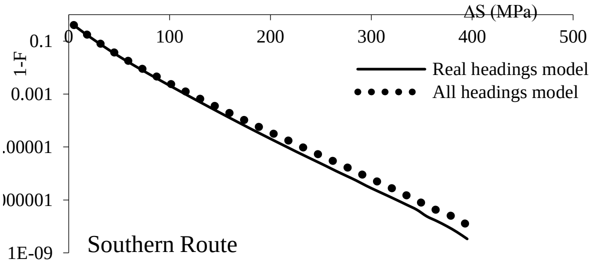

Fig. 3. Long term exceedance probability of stress experienced by a ship which sails in the south route.

4. Fatigue Assessment

4.1 Cumulative fatigue damage

The fatigue life under random loading is calculated based on linear cumulative damage (Palmer-Miner's rule) during 10 years, $D_{10years}$. In Table 1 it is shown that the differences in cumulative damage is about 4% in the northern route, while the difference is about 10% for the southern route, if the all headings and real headings models results are compared.

Table 1. Comparison of fatigue damages in 10 years calculated by storm model and DnV CN. 30.7.

Route	North		South	
Directional model	Real-headings	All-headings	Real-headings	All-headings
$D_{10YR\text{-}mean}$	2.84	2.94	1.62	1.79
L_{fmean} (year)	3.51	3.39	6.15	5.57

4.2 Fatigue crack propagation lives

The fatigue crack propagation (FCP) analyses are performed by using FASTRAN-II, which is based on the crack closure concept. Let *c* and *a*, be the depth and half surface length of a half-ellipsoid crack, and *t* the base plate thickness. An initial surface crack with $c=a=0.2$mm is assumed because this is the minimum detectable crack size. The stress intensity factors (SIF) at the deepest point and the crack mouth are calculated by WES2805 formula. For the target joint, the main plate thickness *t* is 12mm. Let L_P denote the crack propagation life up to the base plate penetration. The structural stress concentration factor, K_S, is set to 1.52 so that the mean L_P becomes comparable with failure lives, L_f, estimated by fatigue damage calculations.

The statistics of calculated L_P are listed in Table 2, which shows that there is a tendency that the crack propagation retardation for real headings model is stronger than that for all headings model. This is because excessive loads occur more frequently in real headings case than in all headings case. Let $L_{P,AH}$ and $L_{P,RH}$ be L_P for all headings and real headings models. In Table 2 is observed that $L_{P,AH} < L_{P,RH}$ for both routes, and the difference is larger in the southern route, on which the difference in P_{EX} (ΔS) is large. Above results show that a substantial difference (at least 16% under conditions chosen) in estimated fatigue life may be encountered when the headings model is changed from the all-headings to real-headings.

Table 2. Comparison of propagation life by FASTRAN II.

Crack propagation life L_P (year)	Northern Route		Southern Route	
	$L_{P,RH}$	$L_{P,AH}$	$L_{P,RH}$	$L_{P,AH}$
Shortest	0.04	0.04	2.86	1.12
Longest	3.89	3.68	11.08	8.24
Mean	2.38	2.05	6.68	4.18
Std. dev.	0.75	0.74	1.67	1.48

5. Conclusions

Fatigue assessments of the welded joint in the 2800 TEU container ship which sails on North Atlantic routes are performed. Two routes with large and small heading angle variations are considered. Stress sequences are generated by Prasetyo's storm model, and the relative heading angle is determined by using all headings and real headings models. S-N analyses based on DnV CN 30.7 and FCP analyses using FASTRAN-II are performed. As results, followings are found:

(1) The difference in heading model affect the fatigue assessment result. The difference in fatigue lives between all-headings and real-headings models is at most about 60% under conditions chosen.

(2) Under conditions chosen, the effect of the difference on SN-based fatigue assessment is small, compare to those obtained in estimated fatigue propagation lives.

(3) Further researches on the development of advanced wave load sequence model which can take into account weather routing and whipping / springing vibration is needed.

6. References

1) Tomita Y., Hashimoto K., Osawa N. 2002. ASTM STP 439.
2) Tomita Y., Kawabe H., Fukuoka T. 1992. Proceeding of 6th PRADS, vol. 2, 1992, pp. 2792-2805.
3) Tomita Y., Matoba M., Kawabe H. 1995. Marine Structure, Vol.8, 1995, pp.407-422.
4) Kawabe H., Syuuji O., Masayoshi O. 2003. Journal of the Society of Naval Architects of Japan, 193, 2003, pp.39-47.
5) Prasetyo F. 2013. Ph.D. thesis, Osaka University, Japan.
6) Prasetyo F., Osawa N., Kobayashi T. 2012. Proceeding of 22nd ISOPE Conference IV, pp 709-712.
7) Mao, W., Pratsetyo F., Ringsberg J., Osawa N. 2013. Proceedings of 32nd OMAE Conference, Volume 2A: Safety and Reliability, pp v02at02a010.

Prediction of Distortion Produced in Welded Structures during Straightening Process using the Inherent Strain Method

Hector Ruiz
Ocean Material Engineering Subarea, Dept. of Naval Architecture and Ocean Engineering

Key Words: *Distortion, inherent strain, straightening, finite element method, Gauss-Legendre quadrature*

1. Introduction

Welding is the most widely used assembly method available to industries in the construction of ships and offshore platforms. However, this method always produces a certain amount of distortion that will not only degrade the performance but also increase the building cost of the structure, and it should be straightened.

Straightening is performed by mechanical or thermal techniques. The principal mechanical technique is pressing, but it is difficult to apply it to 3-D structure such as ship block. Therefore, mainly thermal techniques are adopted in shipyards. These techniques create irreversible strain (inherent strain) into the component. This is achieved by locally heating the material to a temperature where the heated material with lower yield stress expands against the surrounding cold, higher yield strength material, causing compressive plastic strain in the hot material. When the component is cooled, the heated area shrinks and inherent strain is generated. Spot, line or wedge-shaped heating techniques are usually applied in thermal straightening.

In order to optimize the straightening process, it is necessary to predict the distortion due to straightening. Numerical simulation is now reliable and fast allowing efficient study of many cases. Further it does not have the scatter usually found in physical testing. Murakawa [1] developed a thermal elastic plastic based and inherent strain based welding simulation FE code JWRIAN. Coarse shell FE elements are used in JWRIAN analyses.

This drastically reduces the manpower needed for modeling and computer resources needed for calculation, and practical application of welding simulation in production shop floor has been realized. However, it is not easy to perform straightening analysis using JWRIAN because gas heating's inherent strain distributes over a range much smaller than element sizes suitable for welding simulation. Further heating lines on plate fields may be applied at an angle to stiffeners and therefore to element boundaries. To avoid having to use much finer meshes, it is needed to develop a numerical technique which can calculate the initial strain force due to straightening inherent strain confined within a narrow region.

In this study, Osaka University's inherent strain based welding simulation code JWRIAN is modified so that inherent strain's equivalent nodal forces are calculated in cases where the inherent strain confines within a narrow region whose size is smaller/narrower than element size. The validity of the developed software is examined by comparing rectangular plate's transverse bending due to gas line heating calculated by three-dimensional thermal-elastic-plastic analysis and that calculated by the developed system.

2. Inherent strain

The distortion and residual stress produced during local heating are caused by the irreversible strain (inherent strain) formed during the plastic deformation process [2]. Both distortions and residual stress can be predicted by elastic analysis in which the inherent strain is introduced as initial strain. The total strain ε can be decomposed into the sum of elastic strain- ε^e , plastic- ε^p , thermal strain- ε^T , creep strain- ε^c and phase transformation strain- ε^t Eq. (1). Noting that the deformation and the stress are produced by the total and elastic strain, Eq. (1) can be rearranged into Eq. (2).

$$\varepsilon = \varepsilon^e + \varepsilon^p + \varepsilon^T + \varepsilon^c + \varepsilon^t \tag{1}$$

$$\varepsilon - \varepsilon^e = \varepsilon^p + \varepsilon^T + \varepsilon^c + \varepsilon^t = \varepsilon^* \tag{2}$$

3. Elastic FE based on inherent strain

Normally coarse shell FE elements are used in JWRIAN analyses, four node shell elements are used, Fig. 1. There is a need to develop a numerical technique which can calculate the initial strain force due to straightening inherent strain that is confined within a narrow region. In this study a JWRIAN's subsystem is developed which can calculate the initial strain force due to straightening heating.

In the developed code, the initial strain force vector and element stiffness matrix's non-linear term which includes stress components are integrated using higher order (e.g. 20 x 20 x 6 for 4-nodes shell elements) Gauss-Legendre quadrature while other quantities are evaluated by using ordinary order (2 x 2 x 2) quadrature.

In JWRIAN-HI, the element stiffness matrix and equivalent nodal force due to inherent strain are calculated by the equations below:

$$\left[K_{JL}\right] = \int_V \left[B^b{}_{JM}\right]^t \left[D_{MN}\right]\left[B^b{}_{ML}\right] dV + \int_V \frac{\partial N_J}{\partial x_k}\frac{\partial N_L}{\partial x_j}\sigma_{lk} dV \tag{3}$$

$$\left\{F_{inh}\right\} = \int_V \left[B^b{}_{ML}\right]^t \left[D_{MN}\right][\varepsilon_{inh}] dV \tag{4}$$

where, $[K_{JL}]$ is the element stiffness, $[B^b]$ the nonlinear displacement-strain matrix of Mindlin plate for large deflection problem, [D] the stress-strain matrix, N_J and N_L the shape function, x_i the coordinates, σ_{ij} the three in-plane stress component ε_{inh} the inherent strain and $\{F_{inh}\}$ equivalent nodal force due to inherent strain.

In the developed code, the second term of Eq. (3)'s RHS and Eq. (4)'s RHS are calculated using higher order Gauss-Legendre quadrature (see Fig. 2) while other quantities are evaluated by using ordinary order (2 x 2 x 2) quadrature (see Fig. 1).

A 3-dimensional thermal-elastic-plastic FE analysis of the line heating process of a rectangular thick steel plate is performed, and the calculated 3-dimensional plastic strain components (ε_{xx} and ε_{yy}) on the cross section are given to the shell integration points. This mean that the out-of-plane and shear components (ε_{zz}, ε_{xy}, ε_{xz} and ε_{yz}) are neglected in the Elastic Analysis.

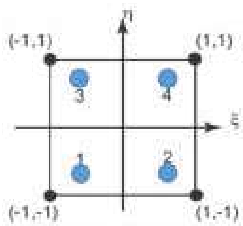

Fig. 1 Shell Element (2x2 Gauss Integration Point)

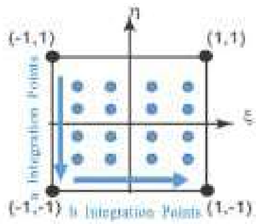

Fig. 2 Shell element (High Order Integration Point).

4. Numerical analysis

Thermal-Mechanical behavior during welding and heat straightening are analyzed using uncoupled thermal/mechanical formulation, Ueda and Yamakawa [3]. However, the uncoupled formation considers the contribution of the transient temperature field to strains and stresses developed through thermal expansion, and temperature-dependent physical and mechanical properties.

5. Interpolation of the inherent strain

Five components of inherent strain (only ε_{zz}.is neglected), are taken from the center of each element once completed the mechanical analysis.

Fig. 3 shows the inherent strain interpolation plotted over the cross sectional inherent strain distribution, for a Gauss integration points arrangement of 4x4x4 points.

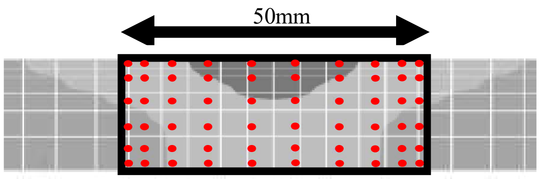

Fig. 3 Gauss integration point arrangement, using high-order.

6. Elastic analysis

The second stage of this research consists in show the effectiveness of JWRIAN-HI, which is verified by comparing the obtained transverse bending angle with TEPA result, while changing element size, Gauss integration point arrangement and heating directions. Fig. 4 shows the Z-displacement comparison between elastic analysis results and TEPA result. Where you can see a large different is obtained, because the edge effect is not considered. Table 6 shows the result when the edge effect is considered. Fig. 5 shows the accuracy of the results with different integ. points, with a max. integ. point space near to 8mm. getting almost constant value until ΔS smaller than 13mm.

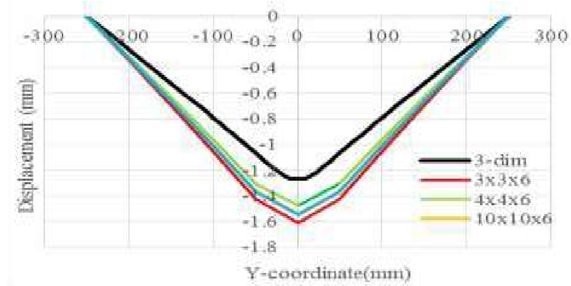

Fig. 4 Z-displacement comparison.

Table 1 Comparison between TEPA and partial heating.

	Maximum Z-Displacement (mm)	Trans Bending (deg)
TEPA	-1.270	0.616
10x10x6_70mm	-1.243	0.609

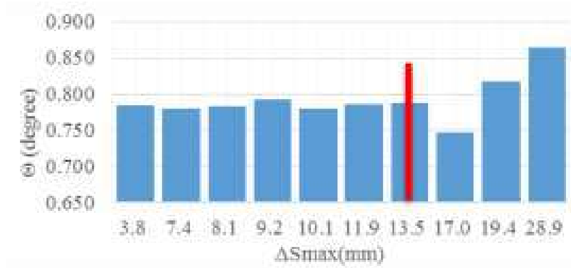

Fig. 5 Max. Gauss integration point space vs theta.

7. Conclusions

It has been demonstrated that the developed element and numerical technique, which calculate the initial strain force due to the straightening inherent strain confined within a narrow region can successfully recreate the three dimensional TEPA behavior.

In this study, it is shown that with a maximum integration point in-plane interval of 13mm or less, the transverse bending becomes almost constant, it means that at least 1/5 of the inherent strain breadth obtained in the TEPA, should have integration points (at least 5 int. points in the heating width) to get accurate results in the elastic analysis.

With the heating conditions used in this study it has been found that shell elements with a width of 50mm is enough to recreate the TEPA, considerably decreasing the computational effort.

References

1) Murakawa H, (2010) "Concept of inherent strain, inherent stress, inherent deformation and inherent force for prediction of welding distortion and residual stress" et al. (Trans. JWRI, 39, 2, pp. 103-105, 2010)
2) Murakawa H, Computational Welding Mechanics and Concept of Inherent Strain for Industrial Applications, Materials Science Forum, 539-543 (207), pp.181-186.
3) Ueda Y and Yamakawa T (1971), "Thermal Stress Analysis of Metals with Temperature Dependent Mechanical Properties, "Transactions of JWRI, 2, No 2, pp.90-10.

Guidance and Control of Autonomous Underwater Vehicle SOTAB-I and Its Application to Data Assimilation

Ryan Putra Dewantara
Marine Mechanical System Engineering Subarea Laboratory,
Department of Naval Architecture and Ocean Engineering

Key Words: *AUV, SOTAB-I, guidance, control, data assimilation*

1. Introduction

Spills and blowouts of oil and gas from the seabed disasters cause enormous damage to the environment as well as to the marine and human life. Early detection and monitoring systems should be deployed around the area where underwater releases of oil and gas first occurred, to prevent them from spreading and causing further damage over time. A rapid inspection of the area by detecting chemical substances and collecting oceanography data could enhance the accuracy of oil and gas behavior prediction or ocean model through data assimilation process. An autonomous underwater vehicle (AUV) called the Spilled Oil and Gas Tracking Autonomous Buoy system (SOTAB-I) was developed to perform in-situ measurements of oceanographic data as well as chemical substances using underwater mass spectrometry (UMS) [1].

The objectives of this research are as follows:

(1) To develop an adequate guidance and control system of SOTAB-I through simulations and field test experiments.

(2) To propose and perform a preliminary study of the application of SOTAB-I to data assimilation.

2. Overview of SOTAB-I

An overview of SOTAB-I is shown in Fig. 1. SOTAB-I is 2.5 m long and weighs 325 kg. It is able to descend in water as deep as 2,000 m and ascend by adjusting its buoyancy using a buoyancy control devices. It can change its orientation through two pairs of moveable wings and move in horizontal and vertical directions using two pairs of horizontal and vertical thrusters.

Fig. 1 Overview of SOTAB-I.

SOTAB-I is equipped with a global positioning system (GPS) receiver and ultra-short baseline (USBL) system for positioning. The vertical position of SOTAB-I in the water is given by depth data from CTD sensor, while at the same time it is also measuring temperature and conductivity (salinity) of the water. The Doppler velocity logger (DVL) is able to measure the robot's altitude and velocities when it is within the bottom tracking altitude from seabed. SOTAB-I's orientation and motion are given by the compass and the Inertial Measurement Unit (IMU). The robot is able to measure the magnitude and orientation of water current layers by using an acoustic Doppler current profiler (ADCP). SOTAB-I is also fitted with a UMS to measure the dissolved gas and oil in the water. Additionally, the robot is equipped with a camera and a stroboscope for taking pictures.

3. Guidance and Control.

3.1 Operational modes

There are three main operation modes in SOTAB-I [2]:

(1) Manual mode
SOTAB-I will be controlled manually through the GUI.

(2) Survey mode
  (a) Vertical water current distribution measurement mode
  The robot measures the water velocity and follows the vertical axis by adjusting its buoyancy level.
  (b) Rough guidance mode
  By repeating descending and ascending on an imaginary circular cylinder centered at the blowout position, the robot collects rough data of water, spilled oil, and gas.
  (c) Precise guidance mode
  Robot will perform detailed measurement by repeating descending and ascending within the plumes.

These modes are based on the depth, altitude, and heading control, which will be discussed in the next section.

(3) Photograph mode
SOTAB-I will move laterally using horizontal thrusters and taking pictures of the seabed around the blowout area.

3.2 Depth and altitude control

In this research, a progressive depth control and altitude control for SOTAB-I was developed, as shown by the block diagram in Fig. 2. The control system is divided into four steps, depending on the robot location during its descending mission:

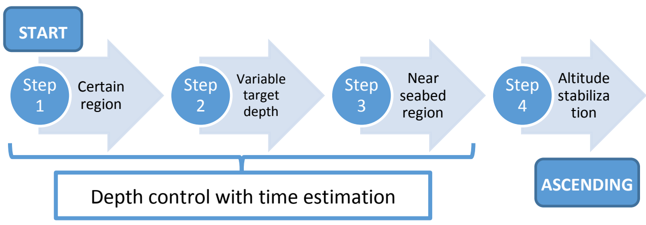

Fig. 2 Block diagram of SOTAB-I depth and altitude control.

Step 1: Safe region between sea surface until a certain depth
Step 2: Deeper region where seabed might be expected.
Step 3: Near the seabed, within the bottom tracking altitude.
Step 4: Altitude stabilization around the set target altitude.

The first three steps adopt the 'depth control with time estimation' method. It controls the output of the buoyancy control device by taking into account the time needed to reach the target depth and for changing the buoyancy level. SOTAB-I will have enough time to adjust its buoyancy level when approaching the target depth or altitude. For the 4th step, the heuristic control method for altitude stabilization is adopted. After a period, it will start the ascending process by increasing its buoyancy level.

3.3 Heading control

The heading of SOTAB-I can be controlled by changing the angle of two pairs of movable wings located on top of SOTAB-I. The wing control formulas for heading control are as follow

$$DELTX = \alpha \sin(\psi_t - \psi) \quad (1)$$
$$DELTY = \alpha \cos(\psi_t - \psi) \quad (2)$$

Where, α is the wing angle, ψ_t is target azimuth, and ψ is current azimuth (yaw). The X direction refers to the East-West direction, while Y direction refers to the North-South direction.

4. Experimental Results

Field experiment was conducted in Toyama Bay on June 11th, 2015, by using a ship of the National Institute of Technology, Toyama College, called Wakashio-maru. The experiment site was located at 36°52'N, 137°11'E with a water depth of around 560 m. The depth control with time estimation scheme was deployed, with a target depth of 400m and target azimuth 60° during ascending. The vertical water current distribution measurement mode was used in the experiment. The results are shown in Fig. 3.

In this experiment was able to smoothly reach the target depth with a slight overshoot of 2.8 m. The experimental result was very similar with the simulation result. As shown by the heading line in Fig. 3, when the heading control was activated during ascending, SOTAB-I was able to stabilize its azimuth at a certain direction. However, there is still some difference with the target azimuth. This might happen due to strong water current effect.

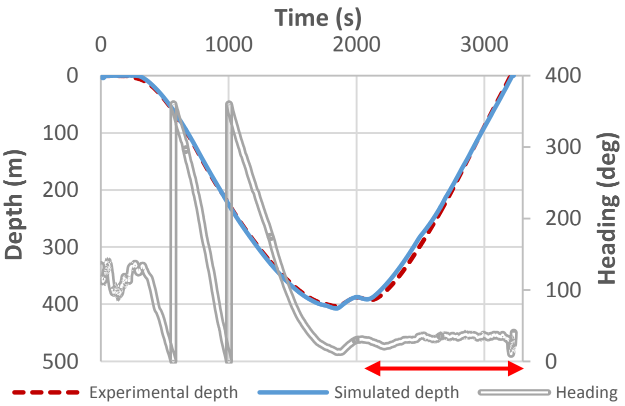

Fig. 3 SOTAB-I Experimental results

5. Data Assimilation

To expand the applications of SOTAB-I, new applications have been proposed in this research. During surveying operation, SOTAB-I is able to collect some oceanographic data and chemical properties of oil and gas. These data can be used for data assimilation to improve the prediction accuracy of: 1) ocean model, 2) oil and gas behavior model. A preliminary study to perform data assimilation of the ocean model has been conducted using Regional Ocean Modeling System (ROMS). ROMS is a free-surface, hydrostatic, three-dimensional model using a terrain following coordinate system for vertical discretization [3]. Data assimilation was performed using incremental four-dimensional variational (I4D-Var) scheme included in ROMS. The model domain covers the U.S. West Coast with resolution 30 x 30 km with 30 vertical layers in the s-coordinate system. The time span is between 3-6 January 2004. Only temperature data obtained from observations by CTD (168 samples, vertically distributed at 10 observation points) and satellites SST (4962 samples, surface temperature, horizontally distributed) were used for data assimilation. The comparison results between free run without data assimilation and with data assimilation are shown in Fig. 4.

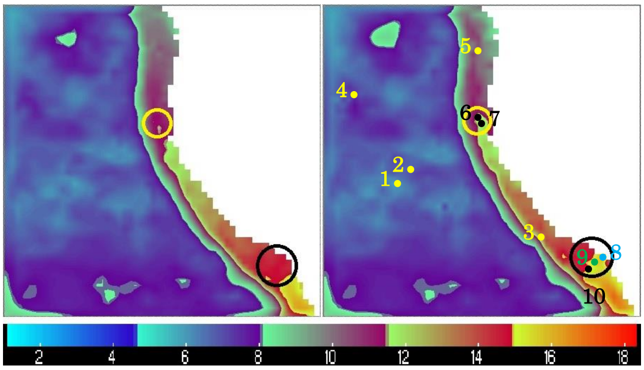

Fig. 4 Results of 4 Jan 2004. Left: free run, Right: assimilated

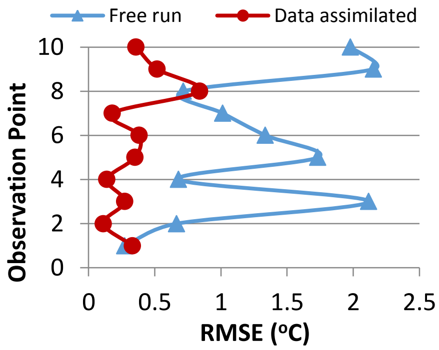

Fig. 5 RMSEs of each CTD observational points

The circled areas in Fig. 4, where some of CTD observations located, show quite significant difference between the free run and data assimilated model. The root mean square error (RMSE) of each observational points have been calculated, and the assimilated model shows in average -60.3% decrease in RMSE.

6. Conclusions

Through guidance and control, the field test results showed that SOTAB-I was able to operate successfully. The depth control simulation was able to simulate similar behavior of SOTAB-I. However, improvements for the heading control should be made.

A preliminary study of performing data assimilation to an ocean model has been conducted. The use of data collected by SOTAB-I for data assimilation might have significant impact.

References

1) Choyekh, M., Kimura, R., Akamatsu, T., Kato, N., Senga, H., Suzuki, H., ...Sakagami, N. ISOPE, Vol.1, pp.695-702, 2013.
2) Choyekh, M., Ukita, M., Kimura, R., Kato, N., Senga, H., ...Sakagami, N. ISOPE, Vol.1, pp.624-631, 2014.
3) Okada, T., Irie, M., Nishida, S. ISOPE, Vol.3, pp.1023-1029, 2014.

Artificial Neural Network Application for Parameter Prediction of Heat Induced Distortion as an Inverse Problem

Cesar De Jesus Pinzon Acosta
Ship Design Laboratory, Department of Naval Architecture & Ocean Engineering

Key Words: *Inverse Problem, Neural Networks, Heat Induced Distortion, Line Heating.*

1. Introduction

For many decades line heating has been used as a method for forming three dimensional surfaces in the shipbuilding industry, however the procedure is often done manually depending on the skill of experienced workers. Therefore this dependency results in a low productivity rate for shipyards which leads to high cost. The prediction of the distortion produced by line heating have been studied for several years. However, it is a highly nonlinear problem consisting of many factors such as the amount of heat, the plate thickness, the speed of the heating source and secondary factors like the cooling method, residual stress, etc. [1]. In order to analyze this phenomena it is required to have an appropriate mathematical tool dealing with all the variables involved in this problem.

Finite element method (FEM), through a three dimensional thermal elastic plastic analysis, is the tool for it, but due to the complexity of the problem, it takes long computational time [2]. Final plate deformation have been successfully predicted by using an ANN model [3], however this ANN model is only able to predict the final deformation of a flat plate due to a line heating process. By this limitation, the ANN model cannot be used to predict the required heating conditions to produce an arbitrary deformation in the plate, which is often requested, in the shipbuilding industry. In this study in order to improve this problem, another ANN model is proposed and discussed.

2. Gas Heating FEM Analysis

The process of forming a plate for a given heating conditions can be viewed as the process to deform a plate into a desired shape by giving the heating conditions, using the shrinkage and the angular distortion induced by the heating and cooling process.

In order to get an accurate representation of the line heating process, a thermal elastic plastic FEM analysis is performed, where a gas heating torch proposed by Osawa et al. [4], is modeled as the heat source model. Thermal elastic plastic analysis can be divided in two steps: the thermal analysis, where the heat source is applied to the model and the mechanical analysis where the four inherent deformation components are obtained.

In this study, square plate model (1200 mm) is generated for the analysis. Moreover the attention is focused in the process of deforming plates with a thickness from 10 to 50 mm as they are more difficult to deform by using the line heating process. Considering that, the maximum temperature of the plate should be kept below 800 C [5], the effect of the heating speed with the surface temperature is evaluated. As a result, the heating speed used to train the ANN model is restricted to a range over 12 mm/s.

3. Forward and Inverse Problems

In the case of the thermal elastic plastic analysis, the model is able to predict the inherent distortion for a given plate thickness and heating speed. This type of problems, where the cause is given and the effect is determined is known as forward problem as it is presented in Fig. 1. On the other hand the prediction of the heating speed by using the actual deformation of the plate and its thickness is an inverse problem where the effect is given and the cause is estimated.

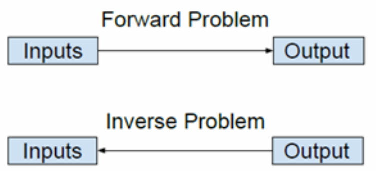

Fig. 1 Forward and Inverse Problems.

Inverse problems is generally difficult, because it may not have unique solution, furthermore inverse problem has a deductive nature rather than the inductive nature of forward problem. To overcome this situation ANN is used based on its ability to approximate unknown input-output mapping.

4. Artificial Neural Network Development

To perform the inverse problem analysis, the ANN model uses the inherent distortion predicted in the forward problem as shown in the Fig. 2. From the figure, it can be seen that the plate thickness is taken as an input parameter since the plate thickness is known beforehand as well as the inherent deformation components, then the ANN model will be able to predict the heating speed required to deform the plate with the desired conditions.

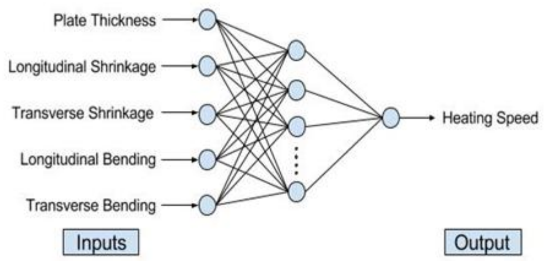

Fig. 2 Proposed ANN model.

4.1 Topology

The performance of the ANN model will depend on the chosen topology. For simplicity of the ANN model, one hidden layer is selected as it is shown in Fig. 2, the number of neurons in the hidden layer is evaluated so as to get the best performance of the ANN model. After evaluating several models, it is noticed that beyond five neurons in the hidden layer, the performance of the ANN model does not improve drastically, thus five neurons are selected for the hidden layer.

4.2 Training Data

The training data play a key role in the development of the model. During the training stage of the ANN model, it is noticed that not only the size but also the quality of the data have a positive impact in the performance of the model.

Once the thermal elastic plastic analysis is completed, the results are evaluated to discard the noisy data. As a result, 120 cases are selected as the training data. Then the data is normalized to enhance the training process. Besides the training data, another set of data is prepared for the purpose of testing the tolerance of the model (unseen set), i.e. this set is not used to train the network, but to confirm the performance of the untaught cases.

5. Model Validation

Considering that the training data is divided randomly into three subsets each time the ANN model is trained, different neural networks trained on the same problem can give different outputs for the same input. Thus several candidates are evaluated in order to select the ANN model with the best performance. Once the ANN model is selected, the response of the ANN model is evaluated in terms of: the training set and the unseen set.

5.1 Training Set

In order to have a complete view of the response of the ANN model, the error generated by predicting the training data is measured and plotted as shown in Fig. 3 from the figure is noticed that the error in the prediction is almost below 2%, thus it proves the good performance for almost the given conditions.

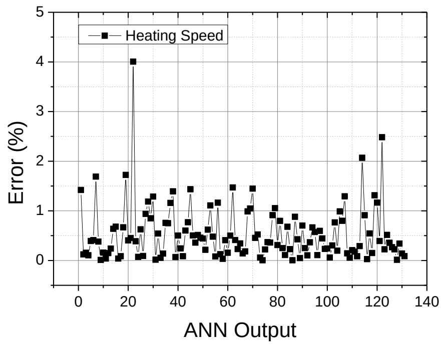

Fig. 3 ANN model response.

5.2 Unseen Set

From Fig. 4, the relationship of the heating speed and the longitudinal bending from a plate of 10 mm thickness is presented, the figure depicts the response of the ANN model for conditions that were not considered in the training data. As it is seen, the response correctly matches with the FEM analysis.

From Fig. 5, the relationship of the heating speed with the longitudinal bending is presented again but this time is evaluated for an 11 mm plate thickness, it can be observed the good estimation of the ANN model for intermediate values of plate thickness. To confirm this results, several cases (square symbols) are calculated by the FEM model for an 11 mm thickness plate. The ANN model has a good capability to predict the heating speed even for untrained cases.

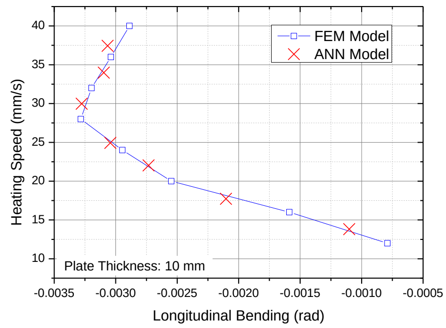

Fig. 4 ANN model prediction for longitudinal bending intermediate points.

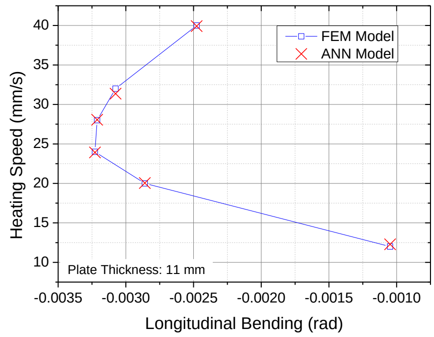

Fig. 5 ANN model prediction for plate thickness intermediate points.

6. Conclusions

The required heating speed for a given plate thickness with certain deformation is accurately predicted by an ANN model through an inverse problem analysis. This model is capable to predict the heating speed by using the plate thickness and the four components of inherent deformation at the middle of the plate. From this study, the following conclusions are drawn:

ANN model can successfully solve line heating distortion as an inverse problem.

The topology and the training data used in the ANN model have greatly affect the performance of the model.

The developed ANN model can successfully predict the heating speed to obtain certain distortion for a given steel plate even for conditions outside the training data.

References

1) Tango, Y, Ishiyama, M, Nagahara, S, Nagashima, T and Kobayashi, J.: Journal of the Society of Naval Architects of Japan, Vol. 193, pp. 85-95 (2003)
2) Vega, A.: Thesis, Osaka University (2009)
3) Pinzon, C., Plazaola, C., Banfield, I., Fong, A. and Vega, A.: Ship Science & Technology, Vol 6, No. 12 (2012)
4) Osawa, N. Hashimoto, K. Sawamura, J. Kukuchi, J., Deguchi, Y. and Yamaura, T.: CMES, Vol. 20, No. 1, pp.45-53 (2007)
5) Blandon, J., Osawa, N., Masanori, S., Rashed, S. and Murakawa, H.: Proc. of The Twenty-fifth IOPEC, Kona, Hawaii (2015)

The Influence of Side Hull Location and Ship Speed on the Ship Wave Pattern of a Trimaran with Wigley Hull Form

Felipe Rodrigues Modesto
Hull Form Design Sub-Area, Department of Naval Architecture and Ocean Engineering

Key Words: *Trimaran, CFD, Ship Wave, Wigley hull*

1. Introduction

Trimarans are well known for applications where high speeds are required. To optimize this effect and the general performance is necessary to know the best arrangement between the main hull and the two side hulls. For this initial study, CFD simulation was used to analyze the wave pattern according the ship speed (Froude number Fn = 0.1, 0.5 and 0.767) and the position of side hulls using η=0.45m and ξ=0m (A1), 2m (C), -1m (D). The test condition and definition of the side hull position (η, ξ) is based on Nozawa at el. (2007) as shown in Fig. 1.

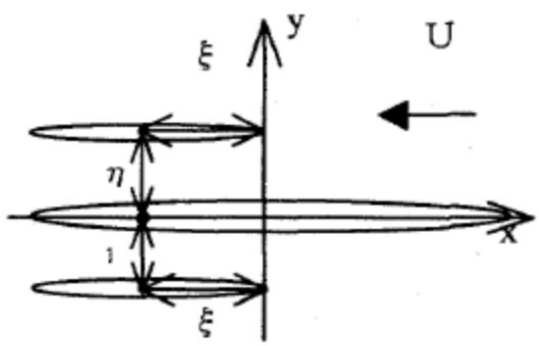

Fig. 1 Trimaran hull arrangement

The trimaran is composed of three Wigley hull was proposed (Nozawa at el., 2007): 2m long main hull and 1m long side hulls. The hull is described as a mathematical equation:

$$y = \pm\frac{B}{2}\left[1-\left(\frac{2x}{L}\right)^2\right]\left[1-\left(\frac{2z}{d}\right)^2\right] \tag{1}$$

where B is the ship beam, L is the ship length and d is the ship draft. (*x,y,z*) is the coordinate point on the ship hull. Firstly, a single Wigley hull will be used to validate the wave pattern.

2. CFD Method

The grid was generated using Gridgen with 7 blocks (two for each hull and the background) in a total of 6.5 million points. The computational domain is defined in -0.5<x<3, -1.5<y<1.5 and -1<z< 0.2 as shown in Fig. 2. About the boundary conditions, the inlet had free stream speed inflow (the ship speed), the outlet has exit condition, the sides boundaries are zero gradient and the top and bottom have far field conditions. The overset grid was assemble using Suggar library.

The software used for viscous flow simulation was CFDSHIP-IOWA V4.5 and it's based on 2nd order finite difference method. With 6 degrees of freedom, in this study only pitch and heave were considered in order to obtain sinking and trim in calm water. The flow field is solved in inertial earth-fixed coordinate and ship motion is solved in non-inertial ship fixed coordinate.

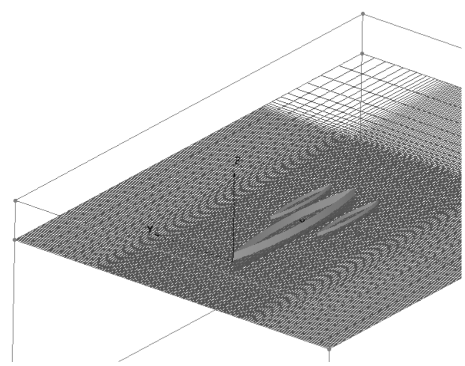

Fig. 2 Computational domain and grid system

3. Results

3.1 Single Wigley Hull

First, a single Wigley hull is used to validate simulated wave pattern and ship wave length. As shown in Fig. 3 the Kelvin wave system including divergent and transverse waves are clear observed. The wave length is a function of the Froude number: $\lambda / L = 2\pi Fr^2$.

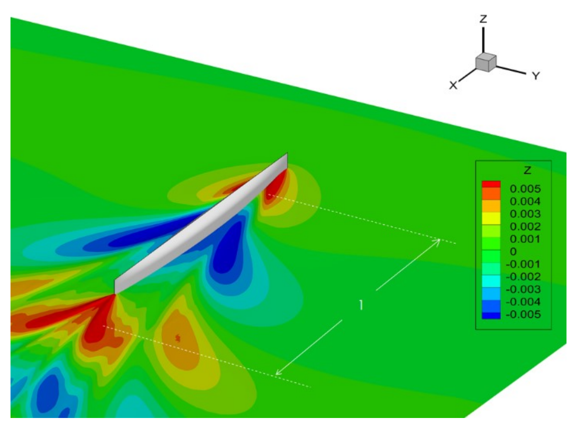

Fig. 3 Wave pattern for a single Wigley hull at Fr=0.767

3.1 Trimaran in different ship speed

In the trimaran case, larger wave lengths as the Froude number increases is observed as shown in Fig. 4. Different from the classic Kelvin wave system, the ship waves generated by the main hull and side hulls would interact. In the highest Froude number, the divergent wave generated in the main hulls bow hits the side hull bow. The wave trough appears between hulls and the large wave trough area in the stern extends downstream at high speeds.

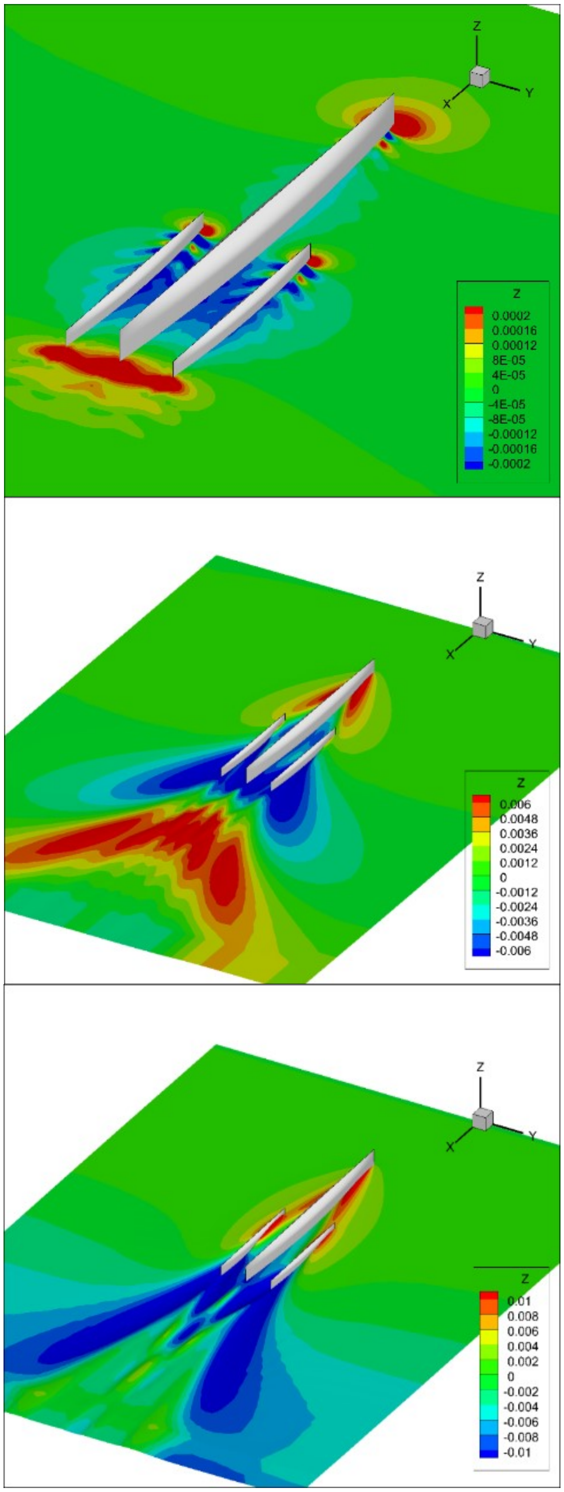

Fig. 4 Trimaran wave pattern at different ship speed: Fr=0.1, 0.5 and 0.767, top to bottom, respectively

3.1 Trimaran with different side hull positions

For different arrangements, A1 hull (ξ=0m) is the same position used in the speed analysis. For C hull (ξ=2m) the side hulls are ahead the main hull and for D hull (ξ=-1m) they are positioned behind the main hull. The distance the main hull and side hull is η=0.45m for all cases. The considered Froude number is 0.767. The results are presented in Fig. 5.

For C hull, the divergent wave crest of the side hull bows extends into the main hull bow. Compared with A1 hull, the wave amplitude is smaller and the wave propagates in smaller area behind the ship. For D hull, the side hulls run in the wave trough generated by the main hull. It implies that the hull wet area is reduced resulting in the lower friction. From the wave pattern observation, we believe the arrangements like C and D hull could reduce the wave making resistance of a trimaran. This was also concluded by Nozawa et al. (2007).

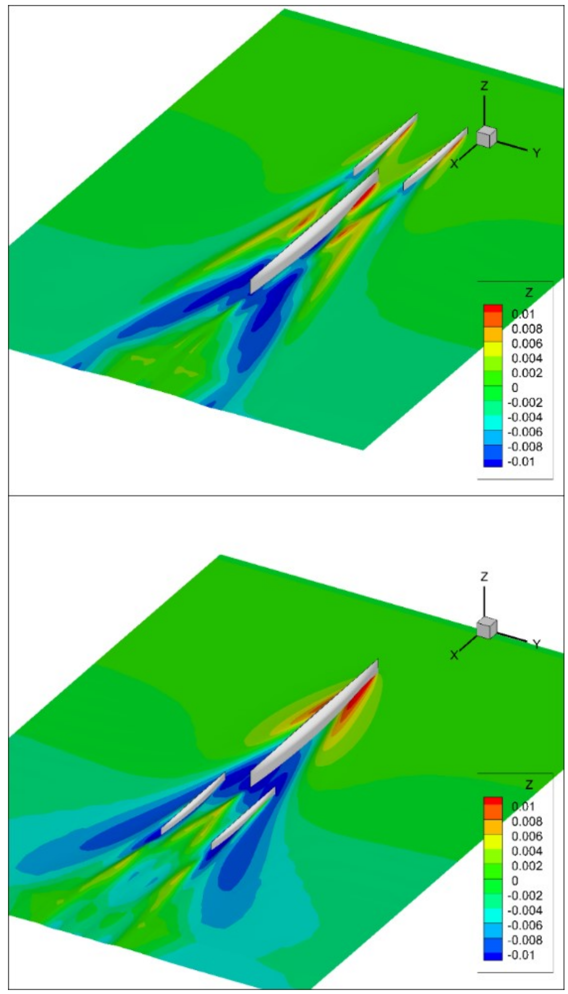

Fig. 5 Trimaran wave pattern for different side hull arrangement at Fr=0.767. Top: C hull; bottom: D hull

4. Conclusions

The wave pattern has been simulated successfully by CFD for single Wigley hull and trimarans. It is possible to reduce the wave making resistance by a proper hull arrangement for a Trimaran.

Reference

1) Nozawa, K., Hayakawa, I., and Tsujiuchi, Y: Conf. of JASNAOE, Vol.4, pp.21-24, 2007.